Scholars' Mine

Doctoral Dissertations

Student Theses and Dissertations

Summer 2015

Iterative CT reconstruction from few projections for the nondestructive post irradiation examination of nuclear fuel assemblies

Muhammad Imran Khan Abir

Follow this and additional works at: https://scholarsmine.mst.edu/doctoral_dissertations

Part of the Biomedical Engineering and Bioengineering Commons, and the Nuclear Engineering Commons

Department: Nuclear Engineering and Radiation Science

Recommended Citation

ITERATIVE CT RECONSTRUCTION FROM FEW PROJECTIONS FOR THE

NONDESTRUCTIVE POST IRRADIATION EXAMINATION OF NUCLEAR FUEL

ASSEMBLIES

by

MUHAMMAD IMRAN KHAN ABIR

A DISSERTATION

Presented to the Faculty of the Graduate School of the

MISSOURI UNIVERSITY OF SCIENCE AND TECHNOLOGY

In Partial Fulfillment of the Requirements for the Degree

DOCTOR OF PHILOSOPHY

in

NUCLEAR ENGINEERING

2015

Approved
Hyoung Koo Lee, Advisor
Xin Liu
Gary Mueller
Ayodeji Alajo
Randy Hays Moss

ABSTRACT

The core components (e.g. fuel assemblies, spacer grids, control rods) of the nuclear reactors encounter harsh environment due to high temperature, physical stress, and a tremendous level of radiation. The integrity of these elements is crucial for safe operation of the nuclear power plants. The Post Irradiation Examination (PIE) can reveal information about the integrity of the elements during normal operations and off-normal events. Computed tomography (CT) is a tool for evaluating the structural integrity of elements non-destructively. CT requires many projections to be acquired from different view angles after which a mathematical algorithm is adopted for reconstruction. Obtaining many projections is laborious and expensive in nuclear industries. Reconstructions from a small number of projections are explored to achieve faster and cost-efficient PIE. Classical reconstruction algorithms (e.g. filtered back projection) cannot offer stable reconstructions from few projections and create severe streaking artifacts. In this thesis, conventional algorithms are reviewed, and new algorithms are developed for reconstructions of the nuclear fuel assemblies using few projections. CT reconstruction from few projections falls into two categories: the sparse-view CT and the limited-angle CT or tomosynthesis. Iterative reconstruction algorithms are developed for both cases in the field of compressed sensing (CS). The performance of the algorithms is assessed using simulated projections and validated through real projections. The thesis also describes the systematic strategy towards establishing the conditions of reconstructions and finds the optimal imaging parameters for reconstructions of the fuel assemblies from few projections.

ACKNOWLEDGMENTS

TABLE OF CONTENTS

LIST OF ILLUSTRATIONS

LIST OF TABLES

LIST OF ABBREVIATIONS

Symbol	Description
AFIP	ATR Flux In trap Position
AIR	Algebraic Image Reconstruction
ART	Algebraic Reconstruction Technique
ASD-POCS	Adaptive Steepest Descent- Projection Onto Convex Sets
ATR	Advanced Test Reactor
ATV	Anisotropic Total Variation
BP	Back Projection
CGP	Channel Gap Probe
COSAMP	Compressed Sampling Matching Pursuit
CS	Compressed Sensing
CT	Computed Tomography
DP	Discrepancy Principle
EM	Expectation Maximization
ERP	Exact Reconstruction Principle
FBP	Filtered Back Projection
FDK	Feldkap-Davis-Kress
GCV	Generalized Cross Validation
GGMRF	Generalized Gaussian Markov Random Field
GMI	Gradient Magnitude Image
GTRI	Global Threat Reduction Initiative

HEU	High Enriched Uranium
HFIR	High Flux Isotope Reactor
HPRR	High Performance Research Reactor
INL	Idaho National Laboratory
LEU	Low Enriched Uranium
MAP	Maximum-A-Posterior
MITR	Massachusetts Institute of Technology Reactor
ML-EM	Maximum Likelihood Expectation Maximization
MRI	Magnetic Resonance Imaging
MRF	Markov Random Field
MTF	Modular Transfer Function
NBSR	National Bureau of Standards
NNSA	National Nuclear Security Agency
NRAD	Neutron Radiography
OS-EM	Ordered Subset Expectation Maximization
ORNL	Oak Ridge National Laboratory
PIE	Post Irradiation Examination
PET	Positron Emission Tomography
PICCS	Prior Image Constrained Compressed Sensing
POCS	Projection Onto Convex Sets
PWLS	Penalized Weighted Least Square
RERTR	Reduced Enrichment for Research and Test Reactor
RMSE	Root Mean Squared Error

ROF   Rudin-Osher-Fatemi

ROMP   Regularized Orthogonal Matching Pursuit

SAA   Shift And Add

SART   Simultaneous Algebraic Reconstruction Technique

SDD   Source Detector Distance

SI   Streaking Indicator

SIRT   Simultaneous Iterative Reconstruction Technique

SOD   Source Object Distance

SEM   Scanning Electron Microscopy

SIR   Statistical Image Reconstruction

SPECT   Single Photon Emission Computed Tomography

SSIM   Structural Similarity

TEM   Transmission Electron Microscopy

TREAT   Transient Reactor

TRISO   Tri-Structural Isotropic

TV   Total Variation

UMRR   University of Missouri Research Reactor

UPRE   Unbiased Predictive Risk Estimate

1. INTRODUCTION

The core components (e.g. fuel assemblies, spacer grids, control rods) of the nuclear reactors experience harsh environment due to high temperature, physical stress, and a tremendous level of radiation. The Post Irradiation Examination (PIE) assesses the integrity of the components released from the power plants. PIE of the irradiated components is performed in three ways, including underwater examination, non-destructive and destructive evaluation inside the hot cells (see Figure 1.1). All data collected from these analyses contribute to the evaluation of in-core reactor performances as well as integrity of the reactor core components.
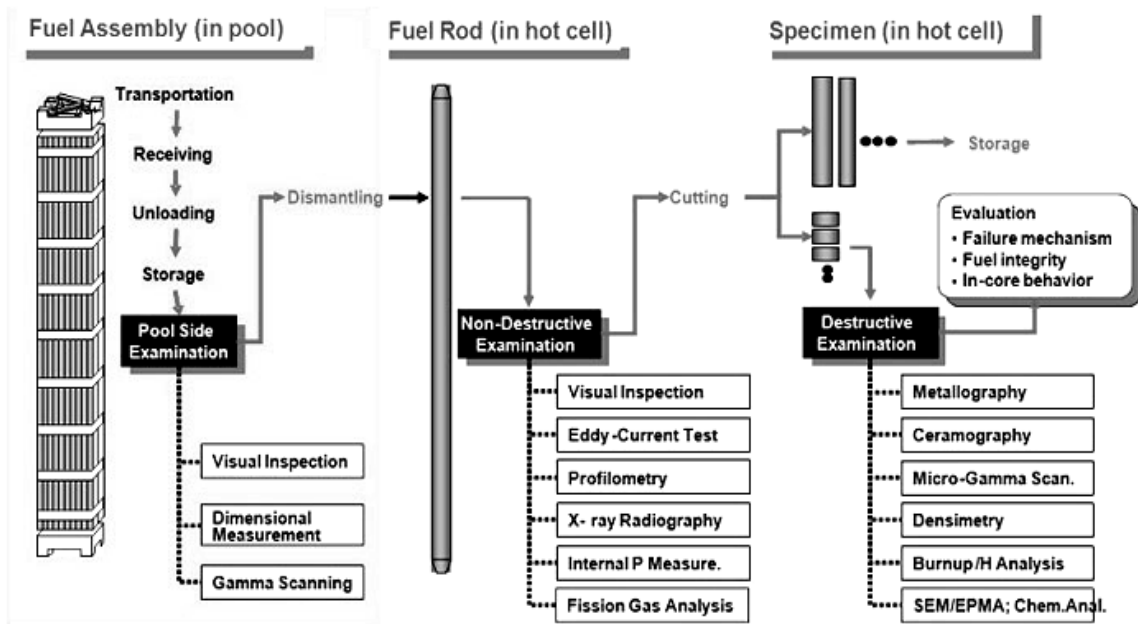
Figure 1.1. The overall PIE process of the irradiated nuclear fuels, as reproduced from [1].

1.1. PROBLEM DESCRIPTION

The National Nuclear Security Administration's (NNSA) Global Threat Reduction Initiative (GTRI) program at the Idaho National Laboratory (INL) develops high-density nuclear fuels converting the high enriched uranium (HEU) fuel to low enriched uranium (LEU) fuel for high performance research and test reactors (HPRR), maintaining equal reactor performance while meeting all safety requirements. This is addressed by the Reduced Enrichment for Research and Test Reactors (RERTR) program [2]. There are five reactors in the United States fall under the HPRR category, including the Massachusetts Institute of Technology Reactor (MITR), the National Bureau of Standards Reactor (NBSR), the University of Missouri Research Reactor (UMRR), the Advanced Test Reactor (ATR), and the High Flux Isotope Reactor (HFIR). Two LEU fuel designs, a dispersion and monolithic type, are being developed (see Figure 1.2) that use a uranium molybdenum (U-Mo) alloy fuel phase.
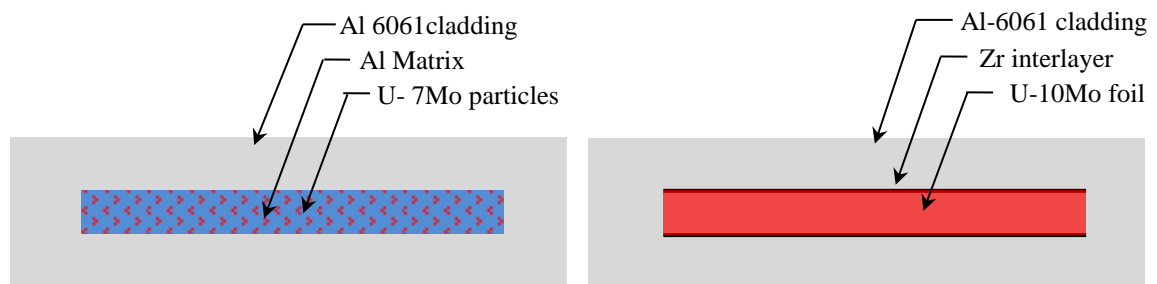
Figure 1.2. Schematic of dispersion (left) and monolithic (right) fuel plate cross-section.

The ATR Full-size in center flux trap position (AFIP) fuel was designed to evaluate the performance a monolithic fuel assembly under irradiation. The fuel assembly has four monolithic foil type fuel plates (see Figure 1.3), composed of U-10 Mo at 19.75 wt.% U-235 enrichment. Each fuel plate has a nominal dimension of 101.60 cm × 6.28 cm × 0.13 cm with a monolithic fuel meat of 97.79 cm × 5.49 cm × 0.0333 cm. The curvature of each plate has a radius of 9.03 cm in the traverse direction. The plate-to-plate coolant channel gap has a nominal spacing of 0.29 cm. The assembly was irradiated for two cycles in the ATR center flux trap between June and November 2011 and several PIEs were conducted. The channel gap was measured using coolant channel gap probe (CGP) to evaluate its structural integrity under irradiation. The AFIP-7 experiment at the INL seeks non-destructive tomographic approach to analyze the behavior of the curved plates under irradiation and to evaluate the second order buckling phenomenon. The tomographic analysis is expected to supersede the local gap measurements made using CGP.

0.13 cm
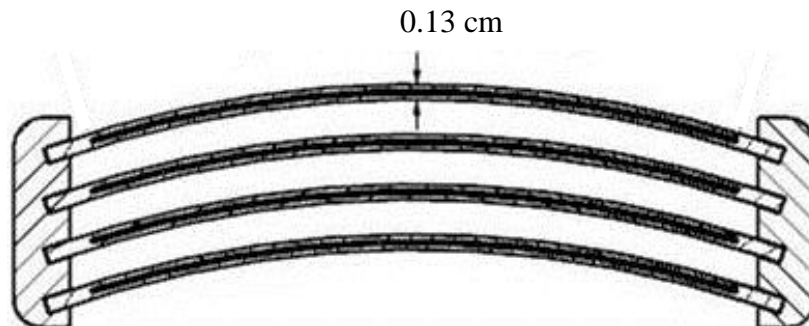
Figure 1.3. Schematic of the AFIP-7 fuel assembly.

The purpose of this research is intended to provide additional strength to the non-destructive PIE of the in-core components using computed tomography (CT). The need for supplemental non-destructive PIE methods is to analyze the structural integrity of irradiated core components and for the early detection of nuclear meltdowns. Additionally, CT may provide useful information to the spent fuel reprocessing facilities for reducing the likelihood of material diversion. If any fuel element is missing from an assembly, CT may provide a means of identifying the missing fuel element.

CT requires an object to be exposed to radiation (e.g. X-rays, neutrons, and gamma rays) from different angular views and acquires projections or radiographs from each view. The contrast in projections depends on the changes in radiation intensity due to attenuation in the object. The attenuation coefficient is a quantity that measures how easily a radiation beam can absorb or scatter across the material it encounters on its passage. A mathematical reconstruction algorithm maps the attenuation coefficients and generates a cross-sectional image of the object from the acquired projections. The cross-sectional reconstructions at multiple axial locations can generate a three-dimensional (3D) reconstruction of the object.

Neutrons differ from X-rays in terms of attenuation. Analyzing irradiated objects with X-ray CT is impossible because the object itself is a strong emitter of X-rays and gamma rays. Neutron CT is useful for the imaging of irradiated objects due to the high attenuation of uranium to neutrons. Typically, digital acquisition systems are widely used for the acquisition of projections. However, it is prohibitive for acquiring images of irradiated samples because the image sensors are very sensitive to gammas.

The INL Neutron Radiography (NRAD) facility utilizes an indirect foil-film

transfer technique for acquiring neutron projections. The technique involves the use of an intermediate detector that produces a projection image upon subsequent processing (see Figure 1.4). A transfer foil (e.g. dysprosium, indium, gold) serves as the intermediate detector and records a latent image through activation of the foil. The activated foil is placed in a dark room and kept in contact with a film for several hours. The decay of beta radiation exposes the film according to the activity pattern of the foil and subsequent chemical development of the film produces a neutron projection image. This technique is insensitive to gamma radiation but requires significant amount of time than the other digital techniques which is prohibitive for acquiring many projections needed for CT reconstruction.

Irradiation	Image Formation
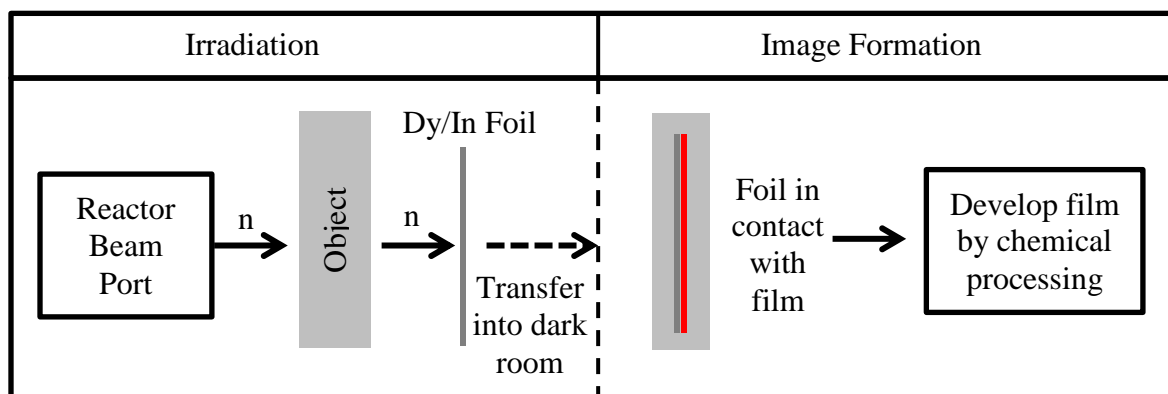
Figure 1.4. Schematic of the indirect foil-film radiography.

The research presented here includes the development of the reconstruction algorithms for analyzing irradiated nuclear fuel assemblies from a small number of

projections. However, if the number of projections is reduced to 100 or less [3], while covering the complete 180˚ or 360° angular range, it refers to as the sparse-view CT. Conversely, if the projections are acquired to a limited angular range instead of covering the full 180˚, it denotes to as the limited-angle CT. The geometries of both modalities are shown in Figure 1.5.
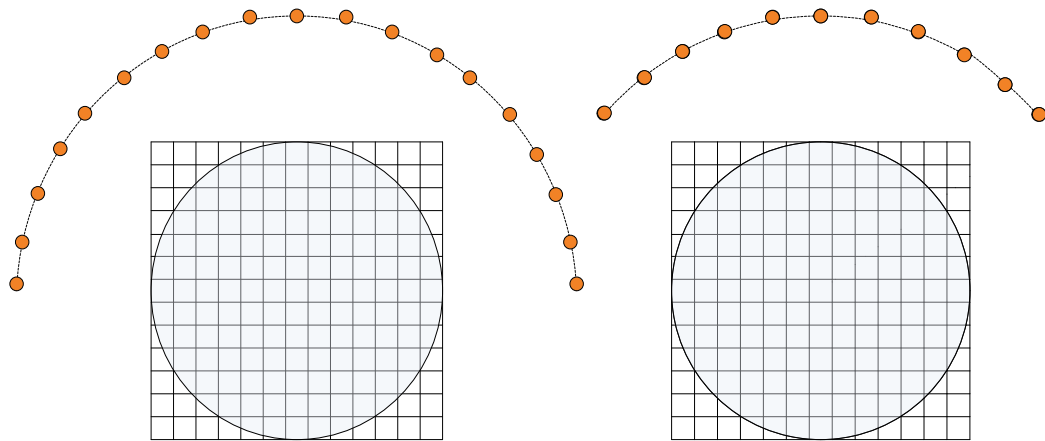
Figure 1.5. Schematic of the sparse-view and limited angle data acquisition.

Tomosynthesis a particular kind of limited-angle CT that reconstructs an image in a quasi-3D image volume [4]. Application of tomosynthesis is popular in many imaging modalities (e.g. dental CT [5], breast tomosynthesis [6] or straight line trajectory [7]) due to the large object size and restricted scanning. Although tomosynthesis reconstruction algorithms can be developed separately, however, all the conventional CT reconstruction algorithms are essentially applicable to tomosynthesis [5] with or without minor modifications.

Iterative reconstruction algorithms are developed for both sparse-view and limited-angle CT in the field of compressed sensing (CS) for the assessment of irradiated nuclear fuel assemblies. The developed CT reconstruction algorithms are evaluated with simulated data and validated through real projections. The thesis also describes the systematic strategy towards establishing the conditions of reconstructions and finds the optimal imaging parameters for reconstructions of the fuel assemblies from few projections. The results show that CT reconstruction from very few projections can be used to identify anomalies, such as missing or substituted elements, gross geometric defects or cracks in the fuel assembly.

1.2. STRUTURE OF THE THESIS

The leitmotif of this thesis is to investigate reconstructions from few projections to inspect the anomalies in the fuel structure, including gross geometric defects, bowing, twist, plate buckling, and cracks. Motivated by an increasing focus on low dose X-ray CT in medical imaging and the limitation of the number of projections in industrial imaging, the sparse-view and the limited-angle CT reconstruction algorithms are developed and evaluated for the inspection of fuel assemblies. The rest of the dissertation is organized as follows: Chapter 2 discusses the principles of radiation imaging, including the physics of X-ray and neutron imaging, and the fundamentals of computed tomography. Chapter 3 discusses traditional CT reconstruction algorithms, including the analytical and the iterative reconstruction methods. The iterative reconstruction algorithm in the field of compressed sensing (CS) is also discussed in this chapter. For solving the CS problem,

particular interest is put on total variation regularization. Chapter 4 describes about the sparse-view CT reconstruction algorithm developed for the inspection of a spent nuclear fuel assembly. The reconstructions of the AFIP-7 fuel assembly for both the sparse-view and the limited-angle CT are described in chapter 5. The optimal imaging parameters to obtain accurate reconstructions from both modalities are also discussed. In chapter 6, the obtained results are discussed before concluding the thesis.

2. INTRODUCTION TO COMPUTED TOMOGRAPHY

The invention of the X-rays by German scientist Wilhelm Röentgen in 1895 and the discovery of neutrons by British scientist Sir James Chadwick in 1932 created a new era of noninvasive radiation imaging. In 1917, Austrian mathematician Johann Radon proposed [6] the principle of reconstruction from a finite number of line integrals. Based on Radon's principle, Allan Cormack and Godfrey Hounsfield [7] invented the first Computed Tomography (CT) scanner in 1972. Currently, CT is an important tool in medical imaging for diagnosing many different diseases. Besides, it has many applications in industrial imaging for detecting defective components and controlling the quality of a production line. The need for noninvasive determination of changes in interior structures of solid objects has supplanted many existing traditional techniques with CT technology.

Although neutron imaging is complementary to X-ray imaging, the fundamental principle of reconstruction remains the same for both modalities. While X-ray CT has wide applications in both the medical and industrial fields, the neutron CT is limited to only the industrial arena. Significant improvements have made over the 42-years of the history of CT developments in terms of speed, slice counts, patient comfort, and resolution. However, it is still subject to active research to obtain an image of sufficiently high quality with minimal exposure and/or cost.

2.1. BACKGROUND OF RADIATION IMAGING

Radiation imaging is a non-invasive imaging technique which produces an image

due to the variation of the transmitted radiation intensity through the object. The radiation intensity varies due to attenuation caused by different structures in the object with varying thickness, density or atomic composition. The X-ray CT utilizes the electromagnetic X-rays while the neutron CT uses neutron particles for imaging.

2.1.1. Fundamentals of X-ray Interactions. X-rays are electromagnetic waves having higher frequencies (*v*) than ultraviolet rays, but lower frequency than that of gamma rays. The radiation is emitted in terms of quanta or photons. Each photon has a defined energy, *hv*, where *h* is the Plank constant. An X-ray of energy more than 100 eV can ionize an atom and penetrate through matters.

X-rays are emitted by electrons and can be generated in different ways; such as from the vacuum tubes or the accelerators. Vacuum tubes use high voltage to accelerate electrons from a hot cathode filament. The high-velocity electrons collide with a target, called the anode, producing X-rays. However, X-rays can be produced in different forms: Bremsstrahlung X-rays or characteristic X-rays. If the high kinetic energy electrons travel very close to the nucleus in the target and is deviated by positively charged electrical field, the electrons lose kinetic energy and Bremsstrahlung (braking radiation) radiation emits in the form of X-rays.

If high kinetic energy electrons cause an electron to liberate from the inner shell of an atom, an electron from the outer shell fills the vacancy of the inner shell. The transition of the high energy electron to low energy electron releases energy in the range of X-ray frequency that is characteristic to each element. However, if the energy is transferred to another electron instead of producing characteristic X-rays, then the electron ejects from the atom. The phenomenon is called the Auger effect, and the ejected

electron is called Auger electron. However, X-rays are generated by accelerating multiple electrons inside the vacuum tube at the same time, resulting in a continuous spectrum of energies as shown in Figure 2.1.

X-ray photons interact with matter in the form of either absorption or scattering. If neither happens, transmit through the object. In the absorption interaction phenomenon, the X-ray photons are absorbed into the object and transfer all their energy to an electron located in one of the atomic shells. If the binding energy of the electron is less than the
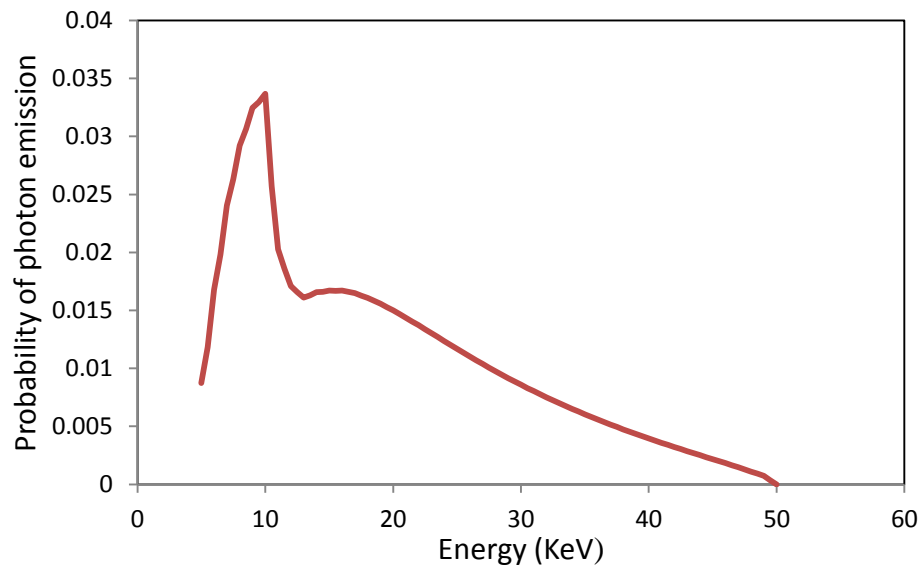
Figure 2.1. Distribution of photon energy created by an X-ray tube voltage of 50 KVp.

energy of the photon, the electron ejects from the atom with a kinetic energy of the photon energy minus the binding energy. This phenomenon is known as photoelectric

(photon-electron) absorption.

Two types of interactions, Compton scattering and Coherent scattering, take place when the X-ray photons interact in the form of scattering. Compton scattering occurs when the photons collide with the loosely bonded outer shell electrons of the atom. The photons transfer part of their energy to the collided electron in which both the energy and momentum is conserved. The incident photons are deflected at an angle due to collision and are scattered from the collision site with energy less than the incident photon energy. The struck electron gains some kinetic energy from the incident photons and recoils.

Coherent scattering occurs when low energy photons collide with a loosely bounded outer shell electron. The incident photons cause the collided electron to vibrate with its frequency. Energy in the form of X-rays, releases due to the vibration of the same frequency and energy as the incident photons. The incident photons deviate during the process cause coherent scattering. However, the rest of the photons, those remaining after absorption and scattering, transmit through the object. The process of removing photons from the beam is called attenuation. In general, the attenuation behavior of a particular material at a given energy is measured by the linear attenuation coefficient or mass attenuation coefficient.

2.1.2. Fundamentals of Neutron Interactions. The electrically neutral directional neutron beam can be generated either from a neutron generating isotope (e.g. neutrons from nuclear reaction) in a reactor facility or from a target in a proton accelerator (e.g. Spallation Neutron Source at ORNL). Similar to X-ray interactions, neutrons interact with matter in the form of absorption or scattering. However, neutron interactions with matter are entirely and ideally complementary to X-ray interactions. X-

rays interact with the orbital electrons of an atom while neutrons interact with the atomic nuclei. X-rays have more interaction probability with increasing atomic number (Z) of matter, but there is no real periodic interaction regularity for neutrons. Isotopes of the same element may differ noticeably in their attenuation ability. Similar to the X-ray attenuation coefficient, the cross section describes the interaction probability of neutrons with matter. The higher cross section represents higher attenuation to neutrons. Depending on the energies, neutrons can be classified as cold, thermal, epithermal, and fast neutrons. Neutron imaging is typically performed in the cold, thermal and epithermal regions due to the large cross sections and detection ability in these energy ranges.

2.1.3. Underlying Physics of X-ray and Neutron Imaging. The attenuation of X-rays or neutrons depends on the type of material and the energy of the incident particles (photons or neutrons). The number of particles removed from the primary radiation intensity is proportional to the number of incident particles (I_0) and the thickness of the object (dx). Thus,

$$dI = -\mu \, I_0 dx \tag{1}$$

where μ is a proportional constant that is known as the linear attenuation coefficient for X-rays and analogous to the macroscopic cross-section for neutrons. It can be defined as the interaction probability of a particle at a particular energy per unit length through a medium. The interaction processes discussed in subsections 2.1.1 and 2.1.2 contribute to the total linear attenuation coefficient of X-rays and neutrons, respectively. The solution of the differential equation (1) is well-known as the Beer-Lambert formula,

$$I = I_0 e^{-\mu x} \tag{2}$$

(2) shows the dependence of the final intensity (I) with an initial intensity (I_0) of the incident radiation and two characteristics of the attenuating medium, the linear attenuation coefficient (μ) and the thickness (x). The exponential nature of attenuation characterizes the intensity of the uncollided particle after traversing through a medium.

In general, the X-rays or neutrons are polychromatic in nature, and the linear attenuation coefficient depends on the energy of the particles. For an inhomogeneous object with different attenuating materials (2) then becomes,

$$I = \int_0^E I_0(E) e^{-\int_0^T \mu(E) dt} dE \tag{3}$$

where T is the total thickness that the particles will travel through the object. The transmitted X-ray or neutron intensity that passes through an object can be recorded in a detector through direct or indirect process yielding a 2D projection image of a 3D object. The contrast of the projection image depends on the attenuation properties of different structures in the object. High contrast X-ray radiography is widely used in medical imaging for analyzing internal structures in the body such as analyzing bone fracture, while high contrast neutron radiography are widely used in industries for inspecting turbine blades, explosive detection, etc.

2.2. BACKGROUND OF COMPUTED TOMOGRAPHY (CT)

Radiography is a useful technique that provides a two-dimensional image of a three-dimensional object. The limitation of radiography is that it cannot provide the cross sectional information of an object and the multiple structures superimpose on the radiograph. CT can generate a 2D cross-section of an object from multiple projections or radiographs. The mathematics to obtaining the cross sectional image is called the CT reconstruction. Starting from data acquisition, the entire process can be categorized into two major steps: one is the data acquisition and sampling, and the other is the data reconstruction.

2.2.1. Data Acquisition and Sampling. Three scanning geometries can be considered for image acquisition, such as parallel beam, fan beam or cone beam geometry. Commercial X-ray CT systems are designed based on fan beam and cone beam geometry. The neutron source from the reactor is assumed to be nearly parallel beam geometry. The reconstructions from parallel beam or fan beam provide the 2D cross section of a slice. With the advent of 2D detectors and faster computers, 3D reconstruction is possible using cone beam geometry.

Typically, CT requires the projection images to be acquired over 180° or 360° of arc acquiring one projection image at each degree. Acquiring many images has several disadvantages. In medical imaging, it increases the radiation dose to the patient. In industrial imaging, it is prohibitively time-consuming and expensive due to longer exposure time. Reducing the total number of projection images (undersampling) degrade the quality of reconstruction and increase reconstruction errors. This will be discussed in detail using sampling theorem in the following subsections. Tomographic sampling refers

to the number of rays per projection and the total number of projections. A brief description of Fourier transform is needed before describing the tomographic sampling.

2.2.1.1 Fourier transform and Fourier slice theorem. The Fourier transform decomposes a function or signal into frequencies. For a 2D object function $f(x,y)$, the Fourier transform $F(u,v)$ is defined as,

$$F(u,v) = \int_{-\infty}^{\infty} \int_{-\infty}^{\infty} f(x,y) e^{-i2\pi(xu+yv)} dxdy \tag{4}$$

During CT image acquisition, the detector and source are assumed to be rotated around the origin at an orientation angle θ, alternately, the object can be rotated with an angular increment θ. Considering a rotated version of the (x,y), the second coordinate system (s,t) can be given as,

$$\begin{bmatrix} s \\ t \end{bmatrix} = \begin{bmatrix} cos\theta & sin\theta \\ -sin\theta & cos\theta \end{bmatrix} \begin{bmatrix} x \\ y \end{bmatrix} \tag{5}$$

The projection $p(s,\theta)$ is generated by drawing a line across x-y plane, orthogonal to the detector and arriving at the detector location s at a particular angle θ. If the projection is defined using delta function, it is known as Radon transform which is formulated as,

$$p(s,\theta) = \int_{-\infty}^{\infty} \int_{-\infty}^{\infty} f(x,y) \delta(x\, cos\theta + y\, sin\theta - s) dxdy \tag{6}$$

where $s = x\, cos\theta + y\, sin\theta$. However, the projection $p(s,\theta)$ can be expressed in terms of

(s,t) coordinate as,

$$p(s,\theta) = \int_{-\infty}^{\infty} f(s,t)dt \tag{7}$$

1D Fourier transform of *p(s,θ)* gives,

$$P(\rho,\theta) = \int_{-\infty}^{\infty} p(s,\theta)e^{-i2\pi\rho s}ds \tag{8}$$

Substituting (7) into (8) yields,

$$P(\rho,\theta) = \int_{-\infty}^{\infty}\int_{-\infty}^{\infty} f(s,t)e^{-i2\pi\rho s}dsdt \tag{9}$$

Substituting (5) into (9), the coordinate system can be transformed to the *(x,y)* system as,

$$P(\rho,\theta) = \int_{-\infty}^{\infty}\int_{-\infty}^{\infty} f(x,y)e^{-i2\pi\rho(x\,cos\theta+y\,sin\theta)}dxdy \tag{10}$$

Comparing with (4), (10) equivalent to the Fourier transform along one radial line, therefore,

$$P(\rho,\theta) = F(\rho\,cos\theta, \rho\,sin\theta) \tag{11}$$

where, $\quad u = \rho\,cos\theta, v = \rho\,sin\theta$

This is known as Fourier slice theorem which states that the Fourier transform of a

parallel projection at an angle θ represents the 2D Fourier transform of the object

function along a radial line (see Figure 2.2) at angle θ in Fourier space.

      2.2.1.2 Sampling for analytical reconstruction. In case of infinite number of projections, the 2D frequency space (see Figure 2.2) will be filled completely. A 2D inverse Fourier transform then yields a reconstructed image in the object space. In practice, infinite number of projections is impossible and only a finite number of projections are available, creating gaps in between two projections as shown in Figure 2.2. However, Reconstruction errors can be caused either by undersampling of data or by the presence of random noise in the measurements. Aliasing artifacts appear in the reconstructed image due to undersampling. The undersampled grid for displaying the reconstructed image can also cause aliasing artifacts. The number of projection images needed for a good reconstruction has been answered by the Shannon sampling theorem. This theorem specifies that a unique reconstruction can be obtained without losing information if the sampling frequency of an object is greater than twice the highest frequency of the object details.
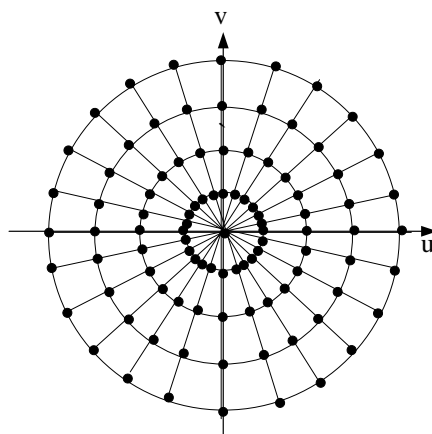
Figure 2.2. Illustration of sampling in Fourier space.

Each sampling point of a projection data represents the data obtained from one detector element, also called one *ray*. As mentioned earlier, each radial line (e.g. P_1P_1' in Figure 2.3) represents one projection in the Fourier space. For sampling using N_D number of detectors, we will have N_D number of rays per projection line. If N_p number of uniformly distributed projections over 180° is necessary toaccomplish the Shannon theorem in parallel beam tomography, then the angular increment $\Delta\theta$ between two successive radial lines in Fourier domain is,

$$\Delta\theta = \frac{\pi}{Np}$$ (12)

For a distance Δx_D between two adjacent rows (detector pixel spacing), the highest spatial frequency (f_N), namely, the sampling points of the outer periphery of the disc, in a projection line that the system can handle is given according to the Nyquist-Shannon theorem,

$$f_{max} = \frac{1}{2}\frac{1}{\Delta x_D}$$ (13)

The distance between any two consecutive rays measured on a radial line P_1P_1' will be,

$$\varepsilon = \frac{2f_N}{N_D} = \frac{1}{\Delta x_D N_D}$$ (14)

The distance (Δf) between two consecutive sampling points (P_1' P_2') on the periphery of the disc is the azimuth resolution which is given by,

$$\Delta f = f_N \Delta \theta = \frac{1}{2\Delta x_D} \frac{\pi}{N_P} \tag{15}$$
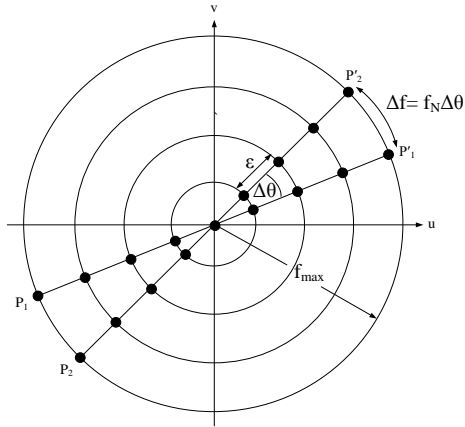
Figure 2.3. Fourier slice theorem pertinent to measured data [8].

A sufficient condition to obtain a good reconstruction is to ensure that, the worst azimuth resolution (Δf) in the frequency domain should be approximately same as the radial resolution (ε). Therefore, we must have $\Delta f \approx \varepsilon$. Thus,

$$\frac{1}{2\Delta x_D} \frac{\pi}{N_P} \approx \frac{1}{\Delta x_D N_D} \tag{16}$$

which reduces to,

$$N_P \approx \frac{\pi}{2} N_D \tag{17}$$

(17) implies that the number of projections needed for a good reconstruction is roughly equal to the number of rays in a projection, in other words, the number of columns in a detector. This statement is independent of any reconstruction algorithm. As a rule of thumb, a CT image should have about as many pixels in each dimension as there are detectors providing data for a view. Therefore, we must have $N_{views} = N_{bin} = N_{pixels}$. Undersampling violates the Nyquist sampling condition which causes the overlap of higher and lower frequency components, which is called aliasing. When an insufficient projection data is acquired, the azimuth spatial resolution becomes poor. However, the pixel resolution, Δx of the reconstructed image derives from the detector pixel spacing Δx_D and the magnification (M). Thus,

$$\Delta x = \frac{\Delta x_D}{M} \tag{18}$$

where magnification is given by the ratio of source detector distance (SDD) to the source object distance (SOD). However, the resolution can be reduced due to the finite size of the source. According to Fourier slice theorem, the complete sampling can be achieved for an 180˚ rotation (see Figure 2.2) of the line with any arbitrary angular interval. The sampling theorem tells us that the detector spacing has to be small enough to record maximum object frequency, in other words, to detect the smallest possible feature.

There are two fundamental cases where limited view angle geometries take place, one is the 2D partial circular scan and the other is the 3D tomosynthesis. In 2D partial scan, the rotation is limited to an angular range of [Φ, -Φ] instead of full 180˚ rotation (see Figure 2.4) which is equivalent to a double wedge with opening angle equal to 2Φ in

2D Fourier space. In 3D tomosyntheis, the source and detector move in an arc along z-axis and the data is represented in 3D Fourier space (see Figure 2.5).

2.2.2. Data Reconstruction. The mathematical procedure of CT reconstruction methods fall into two categories: analytical and iterative reconstruction (see Figure 2.6). The analytical approach can be either using linear algebra or using frequency approach. Two types of frequency approach can be used: Fourier central slice theorem and filtered back projection. Current CT scanner uses filtered back projection (FBP) methods for reconstruction but the quality of FBP reconstruction is highly dependent on the sufficient number of projection images, thus it requires high doses to the patient and significant cost for the industries.

(a) Object space   (b) Fourier space
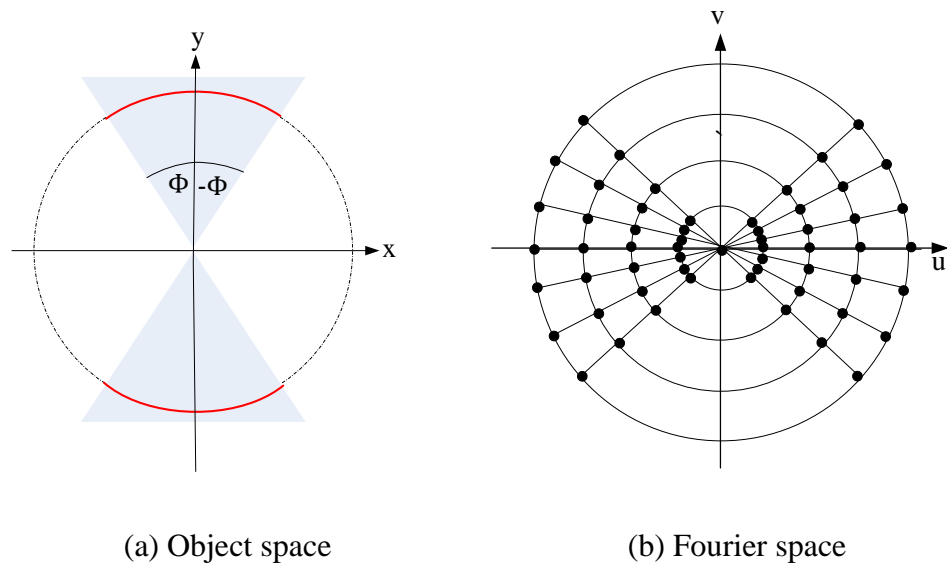
Figure 2.4. Illustration of limited angle sampling (partial circular scan).

Moreover, FBP method assumes that the radiation source is monochromatic, but in real case, the radiation source produces polychromatic spectrum which undergoes beam hardening as it passes through the object. When the polychromatic radiation penetrates through material, low energy radiation attenuates, thus increases effective beam energy and reduces the probability of interaction and creates beam hardening. FBP assumes the attenuation is linear function of material thickness but due to beam hardening, the attenuation becomes a non-linear function. Several beam hardening correction algorithms [9-12] are developed to correct this problem. The corrections can be applied to the projection data prior to reconstruction [9, 10] or can be used after FBP reconstruction [12] as post processing.

(a) Object space   (b) Fourier space
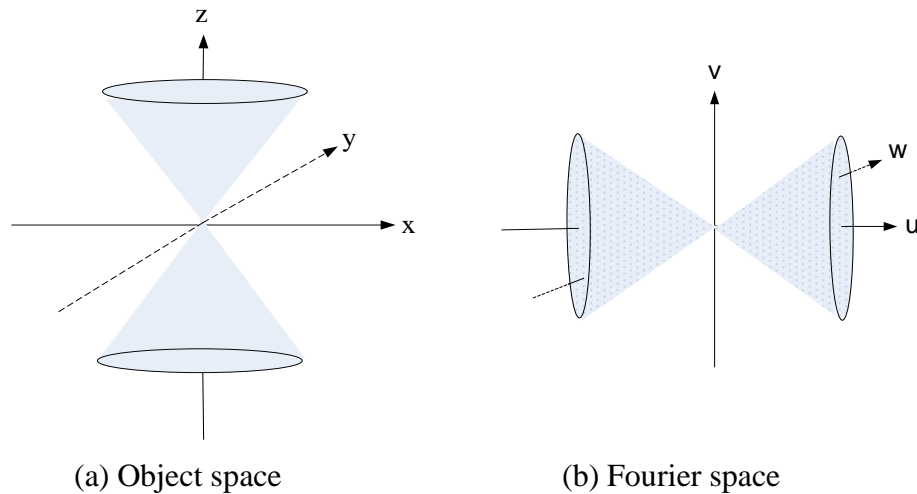
Figure 2.5. Illustration of limited angle sampling (3D tomosynthesis).

However, the radiation dose can be reduced by lowering the X-ray voltage (kVp) or current (mAs). Reducing the number of projection views also reduces the patient

radiation dose as well as cost in industries. In case of incomplete projection data, such as sparse-view CT or limited angle CT, FBP reconstruction often produces artifacts which significantly degrade reconstructed image quality. Compared to the FBP method, iterative methods maintain better image quality by reducing these artifacts while significantly reducing radiation dose and/or cost [13]. Iterative methods are also capable of including physical and geometrical models to represent a more intuitive and natural way of image reconstruction [14].
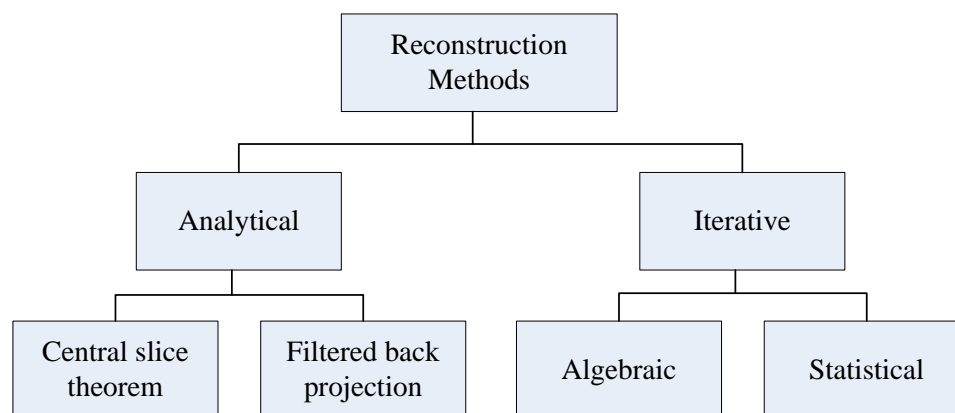
Figure 2.6. Classification of reconstruction methods.

3. CT RECONSTRUCTION METHODS

In this chapter, a detail discussion about the analytical and iterative CT reconstruction methods will be provided. Common reconstruction algorithms, such as Fourier slice theorem, filtered back projection (FBP), simultaneous algebraic reconstruction technique (SART) and statistical maximum likelihood and penalized likelihood approach will be described. The theory of compressed sensing based CT is also described.

3.1. ANALYTICAL IMAGE RECONSTRUCTION

Reconstruction of an exact or approximate image based on analytical transform-inversion is referred to as analytical reconstruction method. Generally, a continuous analytical model is approximated to a discrete model to obtain an approximate inverse of the continuous analytical model. Two types of analytical reconstruction algorithm are widely used for reconstruction: the Fourier slice theorem and the filtered back projection.

3.1.1. Reconstruction Using Fourier Slice Theorem. In Fourier slice theorem, if $p(s,\theta)$ projection data are measured with equal spacing for N number of projections, the reconstruction strategy using Fourier slice theorem is as follows:

- Calculate the 1D Fourier transform of the measured projections,

$$P(\rho,\theta) = \mathcal{F}[p(s,\theta)] \tag{19}$$

- Arrange the Fourier transformed projection in 2D radial lines using,

$$F(\rho \cos\theta, \rho \sin\theta) = P(\rho, \theta) \tag{20}$$

- Resample the data points to a rectangular grid *(u,v)* using interpolation as illustrated in Figure 3.1.
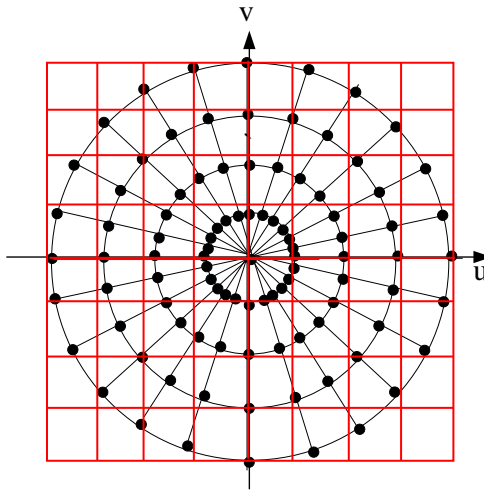
Figure 3.1. Interpolation of Fourier samples into object space.

Perform 2D inverse Fourier transform of $F(u, v)$ to recover the object function using,

$$f(x, y) = \mathcal{F}^{-1}F(u, v) \tag{21}$$

The major disadvantage of the Fourier slice theorem is that, the conversion from

polar grid to rectangular grid creates gridding error due to coarsely sampled data at higher frequencies, producing high frequency artifacts.

3.1.2. Filtered Back Projection. Filtered back projection (FBP) is a reformulation of Fourier slice theorem, yielding a two-step reconstruction method consisting of projection data filtering in the frequency domain and back projection onto image domain. For a 2D object function *f(x,y)*, the inverse Fourier transform *F(u,v)* is defined as,

$$f(x,y) = \int_{-\infty}^{\infty} \int_{-\infty}^{\infty} F(u,v) e^{i2\pi(xu+yv)} du dv \tag{22}$$

where,

$$u = \rho \cos\theta,$$

$$v = \rho \sin\theta, \tag{23}$$

$$du dv = \rho \, d\rho d\theta$$

This yields,

$$f(x,y) = \int_{0}^{2\pi} \int_{0}^{\infty} P(\rho,\theta) e^{i2\pi\rho s} \rho \, d\rho d\theta \tag{24}$$

where $s = x \cos\theta + y \sin\theta$. The outer integral can be splitted into $\theta \in [0,\pi]$ and $\theta \in [\pi, 2\pi]$ and using symmetry properties $F(\rho,\theta) = F(\theta + \pi, -\rho)$ yields,

$$f(x,y) = \int_{0}^{\pi} \left[\int_{-\infty}^{\infty} P(\rho,\theta) |\rho| e^{i2\pi\rho s} d\rho \right] d\theta \tag{25}$$

According to Fourier slice theorem, the 2D Fourier transform of $F(\rho, \theta)$ along the radial line is given by the Fourier transform of the projection $F(\rho, \theta)$. This yields,

$$f(x,y) = \int_0^\pi \left[\int_{-\infty}^\infty P(\rho, \theta) |\rho| e^{i2\pi\rho s} \, d\rho \right] d\theta \tag{26}$$
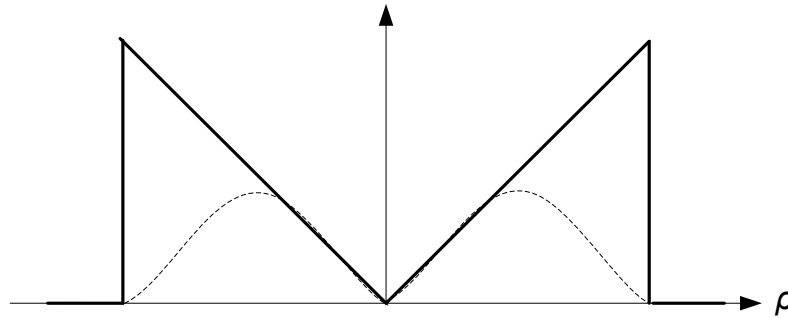
Figure 3.2. Frequency response of Ram-Lak (solid line) and apodization of Ram-Lak filter (dashed line).

In (26), the inner integral is the Fourier transform of the projection data with a projection filtering operation with a filtering kernel $|\rho|$. This is a high pass filter which compensates inhomogeneous sampling. The filter is also termed as ramp filter or Ram-Lak filer and is implemented in discrete form with a cutoff frequency at the Nyquist frequency as shown in Figure 3.2. To avoid the over enhancement of high frequency noise and aliasing artifacts, often a smoothing apodization window function is used, such as Hamming window. The following steps are performed in FBP process:

- Take 1D Fourier transform of the projection data.

- Multiply Fourier transform $P(\rho, \theta)$ with a filter kernel $|\rho|$.

- Take inverse Fourier transform of the filtered projection data.

- Backproject the filtered projections onto image domain.

FBP method is widely used in CT reconstruction if a large number of projection images are acquired over a full angular range. Since corresponding spatial domain is well sampled, FBP produces good quality reconstruction with fewer artifacts. For the cone beam CT and tomosynthesis, the FeldKamp-Davis-Kress (FDK) algorithm, an approximation of the FBP algorithm is used.

3.2. ITERATIVE IMAGE RECONSTRUCTION

The major drawback of analytical algorithms is that, analytical methods are derived assuming continuum of rays. However, in real case, the projection data are finite. Iterative reconstruction (IR) methods model the system based on finite number of measured rays. Iterative methods were first implemented in single photon emission CT (SPECT) in the 1960s [15]. In the early 1970s, the efforts were carried out to transmission CT applications [16]. Other reasons for applying iterative method are that, FBP methods cannot model the physics of the system, including photon statistics, focal spot size, detector response, etc. Additionally, the FBP method assumes that the source is monochromatic; but in practice, the source is polychromatic in nature with different energies leading to beam hardening. Moreover, FBP produces severe streaking artifacts

in the case of few-view reconstruction problem. IR algorithms have been proposed to overcome the problems of FBP. Specially, IR methods can reduce image artifacts and noise in few-view reconstruction problem. Unlike analytical methods where projections are filtered and back projected, IR methods can provide a solution in an iterative manner where the initial reconstructed image is refined and modified iteratively until certain criteria are satisfied [17]. IR methods in CT fall into two categories. One is the algebraic image reconstruction (AIR) method that is based on solving a system of linear equations. The other approach is the statistical image reconstruction (SIR) method that utilizes the knowledge of the underlying physics. SIR methods can incorporate polychromatic sources thus accounting for the beam hardening problem in reconstruction.

3.2.1. Sampling in Iterative CT Reconstruction. In subsection 2.2.1.2, the sampling requirements for analytical CT reconstruction are demonstrated. Sampling requirements for iterative CT reconstruction are different from those for analytical methods. In [18], it has been proven that, for an object containing in a circle of diameter D, if there are N_D number of rays per projection line, then there are a total of $\pi * N_D^2 /4$ unknown pixels inside the object containing the object and only $\pi * N_D /4$ projections are needed to determine the problem by solving a system of linear algebraic equations. The system will be overdetermined if more projections are taken and will be underdetermined if less projections are taken. However, in limited angle CT, the projection data are insufficient to reconstruct the object distribution accurately. Limited angle induces image artifacts and produce geometric distortions characterized by blurring and elongation perpendicular to the direction of the missing projections.

3.2.2. Algebraic Image Reconstruction. Algebraic Image Reconstruction (AIR)

technique is a non-statistical image reconstruction technique. It can model the geometry of the acquisition process better than analytical reconstruction technique such as FBP, thus producing better reconstructions in the case of incomplete projections, such as sparse-view and limited-angle data.

The AIR method solves a system of linear equation $A\mu = y$, where μ are the attenuation coefficients to be reconstructed, y are the measured data or sinogram, and A is the system matrix that characterizes the contribution of each pixel in each line of projection. Typically, AIR methods can be classified into three categories: algebraic reconstruction technique (ART), simultaneous algebraic reconstruction technique (SART), and simultaneous iterative reconstruction technique (SIRT). The reconstruction of the first clinical CT utilized the ART algorithm [16, 19] and generally used the Kaczmarz method [20]. Mathematically, in order to reconstruct an $N \times N$ image from N number of pixels with M number of projections, the line integral of attenuation coefficient is given by a set of linear equation as,

$$\sum_{j=1}^{N} a_{i,j}\mu_j = \ln\left(\frac{I_{i0}}{I_i}\right) = y_i \tag{27}$$

where I_{i0} and I_i are the incident particles and detected particles by detector i, respectively. $a_{i,j}$ is the contribution of pixel j on detector i, where $0 \leq a_{i,j} \leq 1$ and $\sum_{j=1}^{N} a_{i,j} = 1$, μ_j is the attenuation coefficient of pixel j , and y_i is the measured sinogram. where a_{ij} is the contribution of μ_j to y_i, and $i =< 1,2, ..., M >$ is the index of the projection with M total number of projections. (27) can be written in an expanded form as,

$$a_{11}\mu_1 + a_{12}\mu_2 + \cdots + a_{1N}\mu_N = y_1$$

$$a_{11}\mu_1 + a_{12}\mu_2 + \cdots + a_{1N}\mu_N = y_1$$

$$\quad \cdots \cdots \cdots \quad \cdots \cdots \cdots \cdots \cdots \cdots \cdots \cdots \cdots$$ (28)

$$a_{M1}\mu_1 + a_{M2}\mu_2 + \cdots + a_{MN}\mu_N = y_M$$

The attenuation values to be reconstructed and the projections can be written in a column

vector as:

$$\mu = (\mu_1, \mu_2, \ldots \ldots, \mu_N)^T$$

and, $$y = (y_1, y_2, \ldots \ldots, y_M)^T$$ (29)

(28) can be solved by simple linear algebra and is termed as ART [8]. The general

equation becomes,

$$\mu^{n+1} = \mu^n - \frac{a_i\,\mu^n - y_i}{a_i(a_i)^T}(a_i)^T$$ (30)

(30) implies that ART updates the attenuation coefficient values in a ray-by-ray basis and

estimates the voxel values from the difference between the detected and computed pixel

value. The difference is then back projected along the ray and contributes to each voxel

proportional to the path length of the ray inside the voxel. Since the simple ART is

computationally expensive and it takes a single ray at a time, the convergence speed is

very slow compared to FBP. Therefore, the SART method considers one projection at a

time but a relaxation parameter β is added to the update term to reduce the over-

correction of noise and artifacts. This speeds up the convergence speed. The equation in (30) then becomes,

$$\mu^{n+1} = \mu^n - \beta \frac{a_i\,\mu^n - y_i}{a_i(a_i)^T}(a_i)^T \tag{31}$$

In SART, the attenuation coefficients will be estimated after all the rays in one projection are processed. This leads to much faster convergence towards a stable solution. However, a relaxation parameter is needed for the SART method to keep the noise level low and to reduce streaking artifacts [14]. In SIRT, the update is performed after all the projections have been processed. Generally, a positivity constraint is imposed on the pixels because the linear attenuation coefficients are always positive.

The convergence speed is further accelerated by using orders subsets (OS) [21-23] that divide the projections into several groups or subsets and update an estimate for each group instead of updating for the complete dataset. The convergence speed increases with the smaller number of projections per subset. However, the over-correction leads to higher noise and artifacts due to increasing number of subsets. When each subset contains a single projection, the scheme becomes SART, and when one subset contains all the projections, the scheme becomes simultaneous iterative reconstruction technique (SIRT). Since SART contains large number of subsets, the convergence of SART will be much faster than SIRT, and a well-chosen relaxation parameter will keep the noise level and artifacts low and produce good reconstruction results [23]. Another variant of ART method is the multiplicative ART (MART) [24, 25] which multiplies the update with the current solution as opposed to other methods that are additive (or subtractive). A

relaxation parameter is also incorporated with the update term similar to SART. In the AIR methods, the initial reconstructed image is refined and modified until certain criterion is met. However, the AIR methods cannot incorporate the counting statistics of the detected photons; hence it is a non-statistical process.

3.2.3. Statistical Image Reconstruction. Statistical image reconstruction (SIR) methods incorporate knowledge of underlying physics, such as system geometry, detector response, energy dependence and counting statistics of the detected photons into the reconstruction process, offering more accurate and artifact-free reconstruction. Although, SIR methods are widely used in emission tomography such as positron emission tomography (PET) and single photon emission computerized tomography (SPECT), the use of SIR methods in transmission CT are also well established [26-28] specially for few-view and limited angle CT and tomosynthesis. Since transmitted X-ray quanta or neutron particles follow Beer-Lambert's law and the line integral of attenuation coefficient becomes,

$$\sum_{j=1}^{N} a_{i,j}\mu_j = \ln\left(\frac{I_{i0}}{I_i}\right) = y_i \tag{32}$$

where I_{i0} and I_i are the incident particles and detected particles by detector i respectively. $a_{i,j}$ is the contribution of pixel j on detector i, where $0 \leq a_{i,j} \leq 1$ and $\sum_{j=1}^{N} a_{i,j} = 1$, μ_j is the attenuation coefficient of pixel j, and y_i is the measured sinogram. However, number of particles counted by a given detector with a given time interval is assumed to be independent and identically distributed (*i.i.d.*) and the detected

particles follow Poisson distribution. Per Beer-Lambert law, then

$$\sum_{j=1}^{N} a_{i,j}\mu_j{}^* = \ln\left(\frac{I_{i0}}{I_i{}^*}\right) = y_i^* \tag{33}$$

where $I_i{}^*$ and $\mu_j{}^*$ are the expected value of the detected particles and attenuation coefficient, respectively, and y_i^* is the expected sinogram . Therefore, for transmission CT, the probability of receiving I_i, at the expectation value $I_i{}^*$ particles at detector i is given by,

$$P(I_i|I_i{}^*) = \frac{e^{-I_i{}^*}\,(I_i{}^*)^{I_i}}{I_i!} \tag{34}$$

Therefore, I_i corresponds to a Poisson random variable with an expectation value of $I_i{}^*$. For all *i.i.d.* variables, plugging (33) into (34), the probability of receiving all I from M number of detectors becomes,

$$P(I|I^*) = \prod_{i=1}^{M} P(I_i|I_i{}^*) = \prod_{i=1}^{M} \frac{e^{-I_i{}^*}\,(I_i{}^*)^{I_i}}{I_i!}$$

$$= \prod_{i=1}^{M} \frac{e^{-I_{i0}e^{-\Sigma_{j=1}^{N} a_{i,j}\mu_j{}^*}}\left(I_{i0}e^{-\Sigma_{j=1}^{N} a_{i,j}\mu_j{}^*}\right)^{I_i}}{I_i!} \tag{35}$$

$$= P(I|\mu^*)$$

Natural logarithm of (35) yields,

$$\log P(I|\mu^*) = \sum_{i=1}^{M} \left[-I_{i0} e^{-\sum_{j=1}^{N} a_{i,j}\mu_j^*} + I_i \ln(I_{i0}) - I_i \sum_{j=1}^{N} a_{i,j}\mu_j^* - \ln(I_i!) \right] \qquad (36)$$

$\log P(I|\mu^*)$ is the log likelihood function for transmission CT. In classical log-likelihood estimation technique [29], the optimization is obtained by maximizing the log-likelihood of observing I under μ^*, i.e.

$$\mu^*_{LL} = maximize \ (\log P(I|\mu^*) \qquad (37)$$

Various iterative algorithms have been investigated to maximize the log-likelihood function, such as the expectation maximization [30], gradient algorithm [31], etc. The algorithm for iteratively maximizing (37) is called expectation maximization (EM) algorithm. However, CT is a high dimensional inverse problem and sometimes the direct inversion is not possible, therefore, the reconstruction becomes an ill-posed and unstable problem. In order to handle the ill-posed inverse problem, regularization is generally introduced to obtain a modified problem with a unique and stable solution. The statistical regularization technique follows Bayesian model which yields a-posterior probability distribution of μ^* for a given value I. Therefore,

$$P(\mu^*|I) = \frac{P(I|\mu^*)P(\mu^*)}{P(I)} \qquad (38)$$

$P(I|\mu^*)$ denotes as a-posteriori probability density function, which depends on μ^* only.

$P(\mu^*)$ denotes as a prior probability distribution function, which is the probability density function of the original image. $P(I)$ denotes the prior probability distribution of I, which is a constant. Similar to log-likelihood estimation, maximizing log-likelihood of $P(\mu^*|I)$ estimates the maximum a posteriori probability (MAP),

$$\mu^*_{MAP} = maximize\ (log\ P(\mu^*|I)) = maximize(\log P(I|\mu^*) + \log P(\mu^*)) \qquad (39)$$

Therefore, the logarithm of the prior probability density acts as a penalty or regularization functional, which penalizes non-smooth functions in addition to the logarithmic likelihood [29]. Gibbs functions are most frequently used for a-priori probability distribution $P(\mu^*)$ in the form of,

$$P(\mu^*) \sim e^{-\beta R(\mu^*)} \qquad (40)$$

where β denotes a positive parameter and $R(\mu^*)$ is a regularization term. Therefore, the maximization becomes,

$$\mu^*_{MAP} = maximize(\log P(I|\mu) - \beta R(\mu^*)) \qquad (41)$$

Several regularization, including the Tikhonov regularization and the Markov random field regularization are used as the regularization term. However, EM or MAP algorithms are restricted to emission tomography with Poisson distributed data. The M step of EM or MAP algorithm does not produce any close form in case of transmission

tomography [32]. Several modifications [33, 34] are proposed to overcome this problem but the algorithm may still be divergent.

3.3. CT RECONSTRUCTION IN CS FRAMEWORK

As discussed earlier, various analytical and iterative CT reconstruction algorithms are popularly used for image reconstruction from projection data. Candès *et al* [35] and Donoho [36] published the principle of compressed sensing in 2006 which addresses that a large signal or an image can be recovered exactly from much few number of linear measurements through optimization if the signal or the image itself is sparse and noiseless. This integrates the acquisition and compression steps into a single step thus named as compressed sensing.

3.3.1. Background of CS. The conventional sampling theorem states that, one can recover a signal or an image without view aliasing artifacts if the sampling rate is equal or greater to the Nyquist rate. Therefore, it seems that the compressed sensing principle can beat the Nyquist principle. However, the claim is misleading as mentioned in [37] that the CS and Nyquist sampling work under two different assumptions. The Nyquist sampling mentions that a continuous signal can be exactly reconstructed if that is band-limited. The CS reconstruction can only recover a signal completely that is known to be sparse. Although the target images in CT are generally not sparse but if any mathematical transform can make the image sparse then it is possible to reconstruct the image using CS theory. These mathematical transforms are generally called as sparsifying transform which can be used to obtain the sparse image. Generally, the

discrete gradient transform and the wavelet transforms are frequently used as the sparsifying transform [35, 36] to increase image sparsity.

The basic idea of CS image reconstruction process is that if one can reconstruct a sparsified version of the target image from the undersampled data, then an inverse sparsifying transform can be used to transform the sparsified image back to the target image. Since the sparsified image contains fewer image pixels that have significant image values, thus it is possible to reconstruct the sparsified image accurately from the undersampled measurements without any streak artifacts. However, generally the inverse sparsifying transform is not necessary, only the sparsifying transform is needed for reconstruction. An iterative non-linear optimization procedure can be performed instead of inverse sparsifying transform during the reconstruction process. Therefore, the image reconstruction process in CS is the combination of sparsifying transform and the iterative reconstruction algorithm.

The basic idea of CS reconstruction is to solve a constrained ℓ_0-minimization problem as follows,

$$\min_{x} \|\Psi x\|_0 \qquad subject\ to\ \mathrm{A}x = y \tag{42}$$

where Ψ is the sparsifying transform, $\|\cdot\|_0$ is the ℓ_0-norm of the non-zero components of a vector. However, ℓ_0-norm minimization is a combinatorial, NP-hard problem [38] in general and the recovery is not stable in presence of noise [39].

Solving the ℓ_0-optimization problem falls into two basic categories. First is the relaxation of the ℓ_0-optimization via ℓ_1-optimization which is also called Basis Pursuit.

Second is the iterative greedy algorithm such as (Orthogonal) Matching Pursuit [40] and

iterative hard thresholding (IHT) [41]. The advantage of Basis Pursuit is that it guarantees

uniform recovery i.e. it will not fail for any sparse signals while the greedy algorithms

only guarantee non-uniform recovery [42]. Additionally, Basis Pursuit provides stability,

computationally tractable and relies on linear programming. The greedy algorithms are

much faster than Basis Pursuit but cannot provide same guarantees as Basis Pursuit.

Several approaches such as, Regularized Orthogonal Matching Pursuit (ROMP) [43] and

Compressive Sampling Matching Pursuit (CoSaMP) [44] have been studied by

combining both Basis and Matching Pursuit to guarantee the stability as well as speed.

For CT reconstruction, total variation minimization instead of ℓ_1-optimization provides

the sharper image by preserving jumps in the reconstruction as well as geometry of the

boundaries. However, TV minimization can only recover the target image exactly if the

gradient of the underlying target image is sparse and it obeys the ℓ_1-optimization.

3.3.2. Mathematical Formulation of CS for CT. The purpose of CT

reconstruction is to recover μ which contain the attenuation values of each pixel. CS

attracts the image reconstruction community due to its powerful ability to reconstruct

target image from fewer measurements or undersampled data. Several approaches [3, 45-

50] of CS methods have been studied in CT and MRI. The ℓ_1-optimization problem of

(42) can be expressed by,

$$\min_{x}\|\Psi\mu\|_1 \quad subject\ to\ \mathrm{A}\mu = y \tag{43}$$

where the ℓ_1-norm $\|\cdot\|_1$ is the sum of the absolute value of a vector which is also called

the Manhattan norm. μ is the target attenuation coefficients of the reconstructed image.

For an N-dimensional vector μ, the ℓ_1-norm is defined as,

$$\|\mu\|_1 = \sum_{i=1}^{N} |\mu_i| \tag{44}$$

In most practical situations, the acquired data is not perfect and the signals and measurements are corrupted by noise. The drawback of (43) is that the noise is not modeled. Therefore, the optimization problem is modified to allow perturbation and can be reformulated by incorporating error vector in ℓ_2-norm with $\|\varepsilon\|_2 \leq \delta$ as,

$$\min_{x} \|\Psi\mu\|_1 \qquad subject\ to\ \|A\mu - y\|_2^2 \leq \delta \tag{45}$$

where δ is the parameter which controls data fidelity. The constrained minimization problem can be converted into unconstrained minimization problem using Lagrangian approach. Thus, we get,

$$\min_{x} \lambda\|\Psi\mu\|_1 + \|A\mu - y\|_2^2 \tag{46}$$

where λ is a Lagrange multiplier which is also called as regularization parameter. $\|A\mu - y\|_2^2$ and $\|\Psi\mu\|_1$ in (46) are also called data fidelity term and regularizer term respectively. The data fidelity measures the deviation between the measured data and the forward projected expected data. The regularizer incorporates any prior information about the solution similar to the Bayesian approach. λ controls the trade-off between the regularizer and the data fidelity term. $\|\cdot\|_2$ denotes the ℓ_2-norm or the Euclidean norm of

a vector. For an *N*-dimensional vector μ, this is defined as,

$$\|\mu\|_2 = \sqrt{\sum_{i=1}^{N} \mu_i{}^2} \tag{47}$$

(46) can be considered as a posteriori criterion from Bayesian perspective which estimates μ from the measurements $y = A\mu + \eta$ where η is the noise vector with *i.i.d.* elements. Typical CS assumes the data is subjected to additive Gaussian white noise, but in realistic CT, logarithm-transformed Poisson distributed projection data are obtained from each detector.

3.3.3. Total Variation Minimization. The popular type of sparsifying transform, Ψ used in CT is the total variation [46]. The unconstrained optimization problem in (46) can be expressed in terms of TV as,

$$\min_{x} \lambda\|\mu\|_{TV} + \|A\mu - y\|_2^2 \tag{48}$$

Total variation (TV) minimization was first introduced by Rudin, Osher, and Fatemi [51] in 1992. TV-minimization is widely used in classical image processing in the field of denoising, deblurring, and inpainting [51-53]. The goal of TV-regularization is to recover original noise-free signal from additive Gaussian noisy signal. TV-regularization is successful in many applications for suppressing noise from piecewise constant signal having steep jumps. The ℓ_1-norm of the TV term in the discrete version can be expressed as,

$$\|\mu\|_{TV} = \sum_{i,j} |\nabla \mu| \tag{49}$$

where,

$$|\nabla \mu| = \begin{bmatrix} \nabla \mu_x(i,j) \\ \nabla \mu_y(i,j) \end{bmatrix} \tag{50}$$

and,

$$\nabla \mu_x(i,j) = \mu(i+1,j) - \mu(i,j) \tag{51}$$
$$\nabla \mu_y(i,j) = \mu(i,j+1) - \mu(i,j)$$

(49) is also called anisotropic total variation. However, it is suggested in [35] that, for CT, the norm applied to the gradient image is the TV semi-norm and can be written as,

$$\|\mu\|_{TV} = \sqrt{|\nabla \mu_x(i,j)|^2 + |\nabla \mu_y(i,j)|^2} \tag{52}$$

(52) is called the isotropic total variation. However, the TV semi-norm is not differentiable from the numerical point of view. Regularization is needed to avoid the discontinuities. The minimization of TV with the regularization term is known as smoothed total variation regularization [54] and the TV semi-norm becomes,

$$\|\mu\|_{TV} = \sqrt{|\nabla \mu_x(i,j)|^2 + |\nabla \mu_y(i,j)|^2 + \epsilon} \tag{53}$$

However, in the application of CT, the image is not a piecewise constant signal, thus

significant staircasing or blocky artifacts appears in the reconstruction. Therefore, the reconstructed image is subjected to loose contrast due to over-smoothing [55]. Several TV based methods and their variants have been proposed in the CS framework [56-60]. The problems in (45) and (46) are equivalent but generally it is easier to select δ than λ, because it corresponds to the combined effect of noise and model inaccuracy [61]. However, regularized problems are strongly dependent on regularization parameter, λ. Selecting λ manually sometimes provide unsatisfactory solution. Several techniques have been studied [62] to automate λ, including generalized cross validation (GCV), Morozov's discrepancy principle (DP) and unbiased predictive risk estimate (UPRE).

  3.3.4. Optimization Algorithms. As mentioned earlier, CT reconstruction in CS can be achieved in two forms, either a constrained minimization problem that minimizes TV objective function within small and fixed data fidelity, or an unconstrained minimization problem that minimizes the data fidelity error until a certain tolerance is achieved in the TV minimization process. The numerical solution of the constrained and unconstrained minimization is an optimization problem. There are a huge number of algorithms available in the literature but there is no unique optimization algorithm available for CT reconstruction. It depends on the accuracy needed in that particular application. However, the reconstruction is obtained by solving the optimization algorithm iteratively. The optimization algorithms include first order method and their variants, such as steepest-descent or gradient method [63] and accelerated first order method proposed by Nesterov [64]. These optimization algorithms are designed for smoothed TV-functional as mentioned in (53). The subgradient methods are developed for non-smooth TV-functional [65]. Several methods including primal dual methods [66],

homotopy methods [67], dual formulation [52], second order cone programming [68], Bregman distance method [69], graph cut methods [70], and alternating direction method of multipliers [71] are also popular optimization algorithms.

3.4. EVALUATION OF CT RECONSTRUCTION

The image quality in CT depends on several factors, including image contrast, spatial resolution, image noise, and artifacts. These factors determine the sensitivity, which is the ability to perceive low-contrast structures, and the visibility of image details. However, image quality measure has two effects: fidelity and intelligibility. Fidelity describes how the reconstructed image differs from the original image, with root mean-square-error (RMSE). Intelligibility refers the ability through which the image can offer accurate information.

The fidelity of the image reconstruction algorithm is evaluated using RMSE which quantifies the reconstruction error mathematically. RMSE is defines as,

$$RMSE = \sqrt{\frac{\sum(I_{rec} - I_{ref})^2}{(I_{ref})^2}} \tag{54}$$

where I_{rec} is the reconstructed image, I_{ref} is a reference image, and N is the total number of pixel in the image. RMSE evaluates the accuracy of the reconstruction algorithms and measures reconstruction quality. As mentioned earlier, streaking artifact increases due to undersampling in the sparse-view and the limited angle CT. Streaking indicator (SI) is a metric introduced in [72] to quantify the streaking artifacts based on total variation

values. Higher SI value indicates more streaking artifacts, while lower SI value indicates reduced streaking artifacts. We define the SI as,

$$SI = \frac{TV(I_{rec} - I_{ref})}{TV(I_{ref})} \tag{55}$$

where TV is calculated using (52).

The structural similarity (SSIM) index [73] is an effective method of measuring structural similarity between two images. It evaluates the perpetual quality based on the similarity of luminance, similarity of contrasts, and similarity of structures from the two patches of the same spatial window of the two images. Mathematically, the SSIM is defined as,

$$SSIM = \left(\frac{2\mu_x\mu_y + C_1}{\mu_x^2 + \mu_y^2 + C_1} \right) \left(\frac{2\sigma_x\sigma_y + C_2}{\sigma_x^2 + \sigma_y^2 + C_2} \right) \left(\frac{2\sigma_{xy} + C_3}{\sigma_x\sigma_y + C_3} \right) \tag{56}$$

The spatial resolution is a metric for describing the linear and shift invariant system's ability to measure high contrast object of increasingly smaller sizes in the Fourier domain. The spatial resolution is affected by the focal spot size of the source, width of the detector, pixel size, and the properties of the reconstruction filter. Generally, the spatial resolution is measured by modular transfer function (MTF) curve in term of line pair per millimeter using edge method [74].

4. SPARSE-VIEW RECONSTRUCTION OF SPENT FUEL ASSEMBLY

The backgrounds of the classical and CS based reconstruction methods are discussed in Chapter 3. In this chapter, a novel CS based reconstruction strategy is proposed for the sparse-view CT reconstruction of a spent nuclear fuel assembly and compared the results with the classical reconstruction algorithms.

4.1. INTRODUCTION

The advent of compressed sensing (CS) has shown potential over conventional algorithms to generate high-quality reconstruction from the undersampled measurements. It is the most popular method of handling the sparse data. The major significance of the CS theory is that it addresses the sampling condition for exact reconstruction. Mathematically, the CS theory states that an object can be accurately reconstructed from $\sim SlnN$ number of samples to reconstruct an $N \times N$ image from S number of significant image pixels [75]. Conversely, the conventional reconstruction methods rely on Shannon/Nyquist sampling theorem, stating that the number of required samples should be greater than twice the Nyquist frequency of the object.

The statistical image reconstruction (SIR) algorithms provide better reconstructions compared to the analytical and algebraic reconstruction algorithms. The SIR methods model the statistical distribution of the interaction process and estimate the best image from the measured projections. Additionally, prior information can be incorporated to penalize the noise-induced unphysical intensity fluctuations to the neighborhood voxels. For example, the Markov Random Field (MRF) prior based

regularizations, including the quadratic [76] and Gaussian MRF [77], are well-established methods for solving penalized based SIR. However, such regularizations penalize the image irrespective to the information of the underlying structures; hence low contrast information (i.e. fine details) are lost near the edge regions due to over-regularizing [78]. Thibault *et al.* [79] proposed *q*-generalized Gaussian MRF (*q*-GGMRF) prior as regularization to overcome the problem, as well as for faster convergence. However, there is still no agreement on a particular SIR method for CT image reconstruction. Although the statistical methods can provide better image quality than the analytical and algebraic methods, these methods are very difficult to converge to a correct solution. Moreover, the data fidelity term of the regularized SIR method (also called penalized weighted least square, PWLS) is approximated by Gaussian distribution [80] using Taylor approximation.

CS-based image reconstruction from few views is extensively studied in the field of medical imaging to reduce the potential radiation dose delivered to the patients [37, 45, 46, 48-50, 56-59, 75, 80-83]. In the literatures, high-quality reconstructions were produced from few projections using CS strategy. The underlying assumptions to accurately reconstruct an object using CS principle are that the projections should be noiseless, and the reconstructed object should be piecewise constant. However, realistic data are far complicated than the high contrast phantom and contain low contrast information and noisy fluctuations.

In general, the CS algorithms are implemented in the iterative reconstruction framework. The first CS-based CT approach was based on projection onto convex sets (POCS) using constrained total variation (TV) semi-norm minimization. The method

accurately reconstructed piecewise constant object from ~20 view angles [75]. Since the experimental objects are not piecewise constant and often contain low contrast information, therefore, generally more view angles are needed for accurate reconstruction. It is difficult to find an optimal number of projections needed to yield an acceptable reconstruction [84] for a specific object.

TV semi-norm is useful for edge-preserving regularization [85]. The performance of TV-POCS was improved using adaptive steepest descent based POCS (ASD-POCS) algorithm [72, 86]. Several TV based methods and their variants, including anisotropic TV [87, 88], edge preserving TV [83], directional TV [56], and weighted TV [60, 89] were proposed to improve the performance of the algorithm. Prior image constrained compressed sensing (PICCS) [46, 47] and their variants [90, 91] were introduced for dynamic and perfusion CT where a prior high-quality reconstruction is utilized as a constraint in the reconstruction process. The difference between the prior high-quality image and the current estimate serves an additional sparsified transform that enabled significant improvements in the undersampling factors. However, the potential drawback of these algorithms is that they cannot model the noise present in the data [80].

In this work, a new reconstruction technique from few projections is introduced based on CS principle, aiming to reconstruct the spent fuel assembly. The proposed method utilizes simultaneous algebraic reconstruction technique (SART) with total variation (TV) minimization and a dual approach [52] for optimization assuming the projection data are corrupted by Poisson noise. The dual approach avoids smoothing of sharp edges, preserving detail information in the reconstruction as well as suppressing the streaking artifacts. Simulations are conducted to validate and characterize the proposed

method. The qualitative and quantitative studies are performed to evaluate the accuracy of the proposed algorithm. The implementation of the proposed method in real projections demonstrates that it provides reconstruction with improved image quality compared to the reconstruction yielded by FBP and SART reconstruction.

4.2. MATERIALS AND METHODS

Neutron projections of the spent nuclear fuel assembly were acquired at the INL NRAD facility for a series of experiments conducted in the 1980's to evaluate the use of computed tomography as a standard technique for post-test analysis of fuel meltdowns in the TREAT reactor. The fuel assembly consists of 7 fuel rods supported by hexagonal grid spacers at different positions (see Figure 4.1). The assembly was installed in a flowing sodium loop with stainless steel flow tube. The fuel pins were made of MOX fuel with a diameter of ~5mm. The image acquisition geometry was assumed to be nearly parallel with an L/D ratio of 185. The assembly was rotated precisely with 2.4° increments covering 180˚ angular range, with a radiograph acquired at each angle (see Figure 4.2) using the transfer technique [92]. The activity, *A(t),* of the foil is given by,

$$A(t) = \Sigma_a \, \varphi(x, y)(1 - e^{-\lambda t_{irr}}) \tag{57}$$

where, $$\varphi(x, y) = \varphi_0 e^{-\Sigma_t \Delta x} \tag{58}$$

and where Σ_a is the macroscopic absorption cross-section of the specimen, Σ_t is the total macroscopic cross-section of the specimen, $\varphi_0(x, y)$ is the unattenuated neutron beam flux, $\varphi(x, y)$ is the neutron beam flux over (x, y) at the activation foil after passing through the specimen, λ is the decay constant of the activated foil, t_{irr} is the time the foils were exposed to the neutron beam, and x is the thickness of the specimen.

A total of 75 radiographs were obtained using the transfer technique at the hot cell facility. The radiographs are digitized using Genesis NEO S60 film digitizer to a size of 8401×10801 pixels and registered spatially along its center of rotation. The digitizer uses cold cathode lamp as light source that can measure a maximum optical density of 4.7
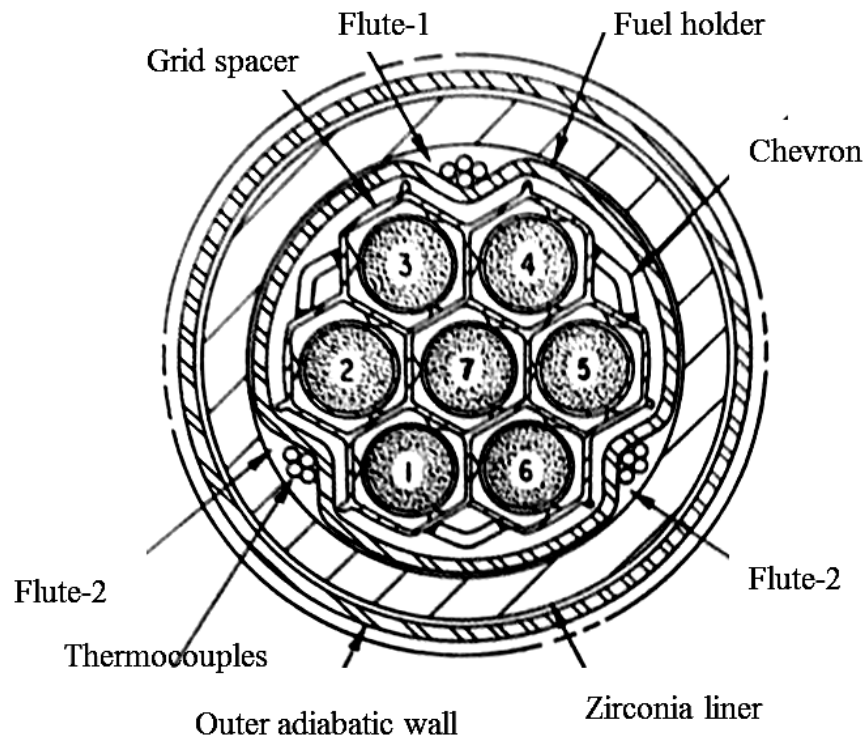
Figure 4.1. Schematic of a cross-section of the spent fuel assembly.
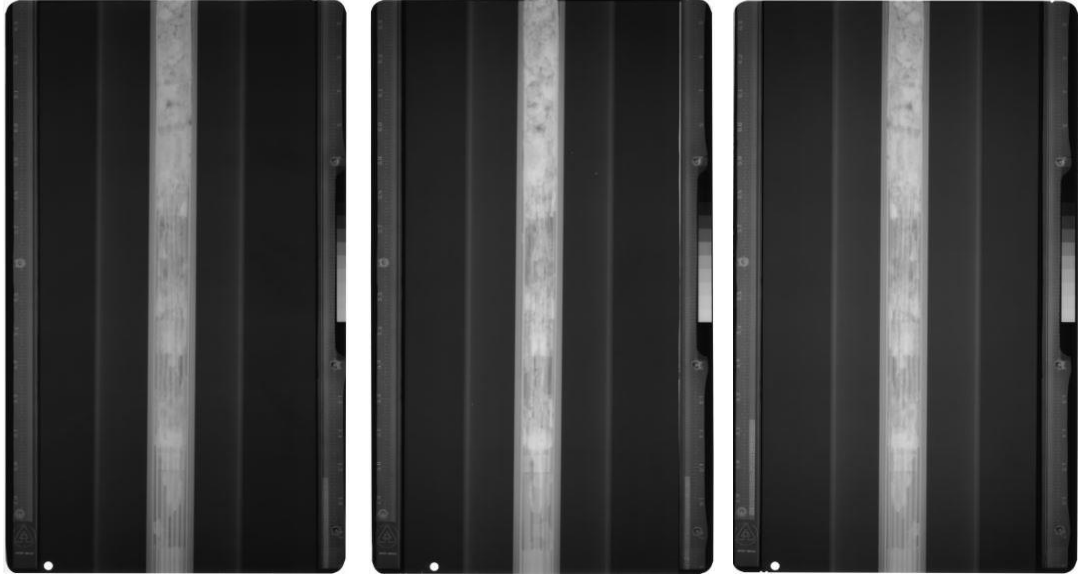
Figure 4.2. Digitized neutron projection images of the spent fuel assembly from three different angular views.

with a spatial resolution of 600 dpi. The scan rate of the scanner is 1.5 milliseconds per line and the total scan time is 55s for a 14 inch × 17 inch film. The size of the neutron radiographs are 25 cm (~10 in.) × 45 cm (~17 in.) but since the scanner software has limited option to select the film size, the scans are performed at 14 inch ×17 inch in size. The digitized projection images were horizontally cropped to 1024× 10801 pixels to remove blank background pixels prior to reconstruction. Several pre-processing steps were performed to spatially co-register the radiographs [92]. When neutrons are captured by the activation foil as discussed in subsection 1.1, the number of beta particles that activates the film is assumed to follow compound Poisson process. Some of the properties and the image acquisition parameters of the fuel assembly are given in Table 4.1.

Table 4.1. Properties of the spent fuel assembly and neutron
image acquisition parameters

Parameters	Value
Fuel composition	UO_2+PuO_2
Fuel diameter (mm)	4.95-5.00
Fuel pellet theoretical density (g/cm^3)	11.05
Irradiated fuel density (g/cm^3)	10.2
Fuel pellet geometry	Annular
L/D ratio	185
Time of exposure (min)	22

The aim of this work is to develop an efficient scheme in the context of CS to accurately reconstruct the spent fuel assembly from 75 projection images with minimal artifacts and noise. In the following subsections, the proposed algorithm is discussed in detail.

4.2.1. Mathematical Formulation. The variational problem for Poisson denoising is given in [53] which is utilized and implemented this into the iterative CT reconstruction framework as,

$$\min_x \lambda \|u\|_{TV} + \int_\Omega (u - f \log u) \tag{59}$$

where u is the image to be reconstructed, f is the measured projection data, $\|u\|_{TV}$ is the TV-semi norm as mentioned in (52). Further approximation of (59) using Taylor

expansion gives the weighted quadratic data fidelity for the Poisson noise as,

$$\min_x \lambda \|u\|_{TV} + \frac{1}{2} \int_\Omega \frac{(u-f)^2}{f} \tag{60}$$

The numerical solution of (60) is given in [93] as,

$$\min_x \lambda \|u\|_{TV} + \frac{1}{2} \int_\Omega \frac{(u-f)^2}{w} \tag{61}$$

where *w* provides the weighted modification of the data fidelity term. A variety of algorithms is used to solve an optimization problem, including projected gradient method [63], homotopy methods [67], dual formulation [52], first order primal-dual methods [66], second order cone programming [68], Bregman distance method [69], accelerated first-order methods developed by Nesterov's algorithm [64], etc. In this work, Chambolle's non-linear semi-implicit gradient descent method [52] is utilized to solve the TV minimization problem, considering an isotropic discretization of the total variation. The advantage of using Chambolle's projection method is that it solves the nonsmooth TV-functional and provides the exact solution with proof of convergence [54] instead of solving the approximation similar to (53). However, Chambolle proposed the optimization algorithm based on standard noise model, considering the image is corrupted by Gaussian white noise. Chambolle's method for the Poisson statistics is reformulated in [93] as,

$$u = f - \lambda w div \tilde{g} \qquad (62)$$

where ,

$$\tilde{g} = minimize \ (\lambda w divg - f)^2$$

and,
$$g^{n+1} = \frac{g^n + \tau \nabla(\lambda w divg^n - f)}{1 + \tau |\nabla(\lambda w divg^n - f)|}, \qquad 0 < \tau < \frac{1}{4\lambda w} \qquad (63)$$

(62) shows that, the primal variable, f of the image data is explicitly expressed with a dual variable $\tilde{g}$ and the dual variable is iteratively computed using (63) to obtain the primal variable.

4.2.2. Proposed Algorithm. The optimization problem in (61) is solved using (62) and (63). The overall process is implemented in a two-step process by combining SART reconstruction into the TV minimization problem. The initial guess for the SART step is assumed to be zero for all pixels. The SART updates the estimated image using (31) by forward projecting the initial image into the sinogram space. Then the difference between the estimated sinogram and the given sinogram is backprojected into the image domain to update the estimated image. This difference is then subtracted from the initial image to obtain a corrected image. A relaxation parameter, β is multiplied with the estimated image at each iteration to suppress the over enhancement of noise and artifacts. In this experiment, a constant β value of 1.5 is chosen. The iterations proceed until a certain stopping criterion is met. A positivity constraint is imposed on the SART step to enforce data consistency and positivity because the negative values do not have any physical significance [75]. The TV step utilizes the result obtained from the SART step as the initial guess for the TV step. The SART step and the TV step runs iteratively in an

alternating manner. The SART is used instead of ART to speed up the convergence. The overall process can be realized as a nested two-step process,

SART step:
$$u^j = u^{j-1} - \beta \frac{A_i u^{j-1} - f_i}{A_i (A_i)^T} (A_i)^T$$

(64)

TV step:
$$u^{k+1} = u^{SART} - \lambda w div \tilde{g}$$

The first order optimality condition guarantees the equivalence of the minimization step with the TV step [94]. The overall reconstruction algorithm can be realized by solving the following variational problem as:

$$u_{k+1} = \min_{\mu} \left\{ \frac{1}{2} \int_{\Omega} \frac{(u - u_{SART})^2}{u_k} + \lambda \|u\|_{TV} \right\}$$

(65)

(65) is equivalent to the Rudin-Osher-Fatemi (ROF) model [51] but with a weight of $1/u_k$ in the data fidelity term. The weight depends on the reconstructed image and serves as a local regularization parameter [53]. The second guess of the SART step is the result obtained from the previous TV update. The implementation steps are shown in Table 4.2.

4.2.3. Regularization Parameter Selection. The selection of regularization parameter, λ is very important to obtain a satisfactory reconstruction from the optimization algorithm. A large parameter cannot provide good convergence while a small parameter will increase the computational time. As mentioned in subsection 3.3.2 that, there are several methods to select regularization parameter. In the proposed

method, λ is chosen according to discrepancy principle (DP) because it is an effective regularization parameter selection method for Poisson statistics [62] compared with the GCV and UPRE. It provides sensible values of λ for the Poisson corrupted data [95]. Discrepancy principle states that the reconstruction should have a mean squared difference from the noisy data that is equal to the variance of the noise. The value of λ is chosen from the initial guess and it changes in every iteration according to DP. The SART step stops when the difference between the RMSE value of the currently estimated image and estimated image of the previous step has a small difference in the order of 10^{-5}. The TV step stops when the difference between the TV value of the current estimate and the TV value of the previous estimate has a small difference in the order of 10^{-5}.

4.3. RESULTS

The performance of the proposed method is evaluated from simulations by obtaining reconstructions from different number of projections with uniformly spaced view angles extracted from 180 views to reveal how the degree of sampling influences the reconstruction. The simulation studies are conducted using 45, 60, and 75 projections and reconstructions are generated using the proposed technique. The qualitative and quantitative studies are conducted to assess the effectiveness of the proposed algorithm. Then the algorithm is applied to reconstruct the spent fuel assembly. The fuel assembly is reconstructed using 75 projections. The reconstructions are compared with the classical BP, FBP and SART method.

Table 4.2. Implementation of SART-TV reconstruction

Proposed Algorithm

Input: τ, β ; **Initialization:** $u^0 = 0$

while (*stopping criteria not satisfied*)

   //SART step

    while $\left|RMSE^j - RMSE^{j-1}\right| < 10^{-5}$

      $u^j = SART\,(u^{j-1})$

    end $u^{SART} = u^j$

   //positivity constraint

     if

        $u^{SART} < 0$

        $u^{SART} = 0$

     end

   // TV step

    while $|TV^k - TV^{k-1}| < 10^{-5}$

      $g^k = \dfrac{g^{k-1} + \tau\nabla(\lambda wdiv g^{k-1} - u^{SART})}{1 + \tau\left|\nabla(\lambda wdiv g^{k-1} - u^{SART})\right|}$

    end $u^k = u^{SART} - \lambda wdiv \tilde{g}$

   $u^{j-1} = u^k$

end

      4.3.1. Simulation Study. The phantom study provides a theoretical understanding

of how well the proposed method performs with few projections. The performance of the

proposed algorithm is evaluated on a piecewise constant fuel assembly phantom that contains 512×512 pixels (see Figure 4.3a). The fuel assembly phantom is simulated based on the geometry of a nuclear fuel assembly. Simulations were first conducted under ideal condition, which means that the sinogram was generated without any presence of noise. Then, the projection data were modeled as a compound Poisson process assuming the particles per pixel is 5×10^6.

  4.3.1.1 Noise-free case. The gradient magnitude image (GMI) of the fuel assembly phantom (see Figure 4.3b) contains 14,818 pixels, which is about 7.17% of the 206,637 non-zero pixels of the original phantom of 512×512 size. According to the CS exact reconstruction principle (ERP), the optimization technique will provide a unique solution if the number of Fourier samples is greater than or twice the number of the non-zero pixels in the GMI. Therefore, the minimum of 2×14,818= 29,636 projection data points are needed to achieve an exact reconstruction. If the projection data points are less
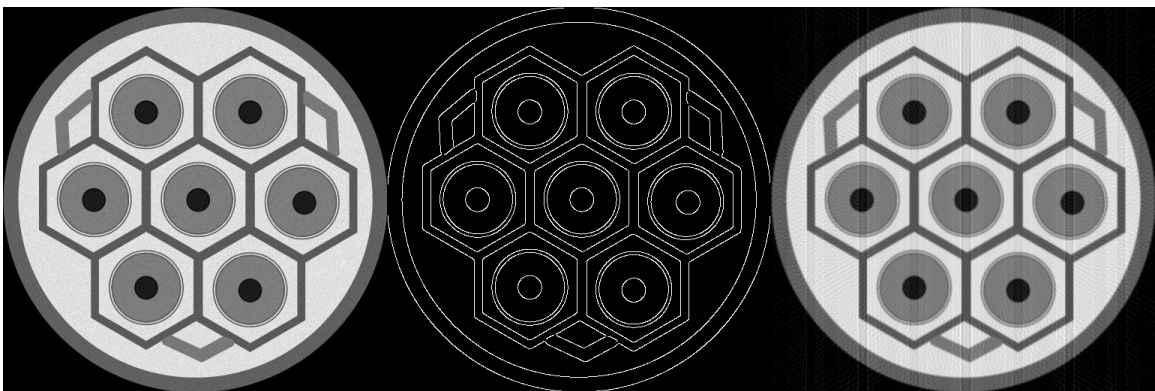

Figure 4.3. Illustration of (a) the simulated phantom of a nuclear fuel assembly, (b) the GMI of the phantom which has greater sparsity than the original phantom, and (c) the reference truth image reconstructed using 180 projections with an angular increment of 1°.

than 29,636 then the system will be underdetermined. For example, with 45 projections, the total number of projection data points is 512×45= 23,040 which is less than the required minimum number of non-zero data points (i.e. 29,636) needed for reconstruction; therefore, exact reconstruction cannot be achieved according to the ERP principle. If we consider 60 projections, the total number of data points is 30,720, which is greater than the minimum data points required. Thus, the fuel assembly phantom can be reconstructed exactly if more than 60 projections are available.

To demonstrate the performance of the proposed method, the phantom was uniformly sampled with 45, 60, and 75 views over 180° range assuming the detector has 512 bins The proposed method is compared to the results obtained from conventional FBP and SART algorithm with equal sampling rate. A reference image is reconstructed using 180 projections (see Figure 4.3c) with an equal spacing of 1°. The qualitative comparison among the reconstructions of the fuel assembly phantom without noise is shown in Figure 4.4. From the visual comparison, it is observed that the FBP method generates severe streaking artifacts in the reconstructed image. The detail structures of the assembly are barely identifiable due to the appearance of these artifacts. SART improves the result, eliminating these artifacts to a certain extent but there are still artifacts present in the reconstructed image. Increasing the number of iteration can reduce some artifacts, but after a certain number of iterations, the reconstruction becomes blurry and generates blocky artifacts. The proposed TV based method effectively suppresses the artifacts and improves the quality of reconstruction compared to the FBP and SART as shown in Figure 4.4.
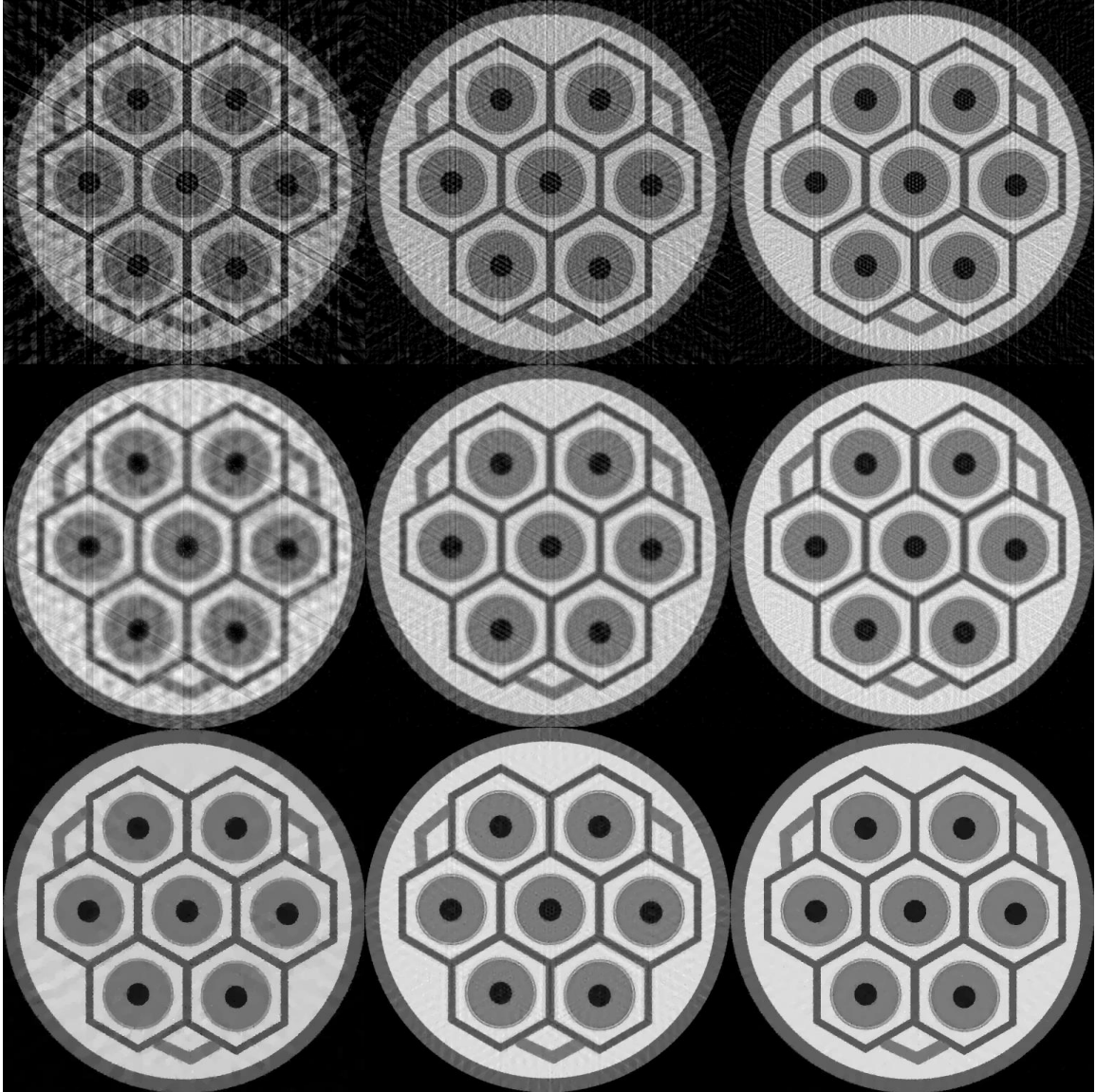
Figure 4.4. Reconstruction of noise-free phantom using the FBP (first row), SART (second row), and TV based CS algorithms (third row) at three different view angle sampling rates: 45 (first column), 60 (second column) and 75 (third column).

A vertical line profile is drawn across the 256th column of each reconstructed images and compared with the line profile of the original phantom as shown Figure 4.5. The profiles demonstrate that the proposed TV based method closely matches with the line profile of the original phantom. Compared with the line profile of the reference

image and the line profile obtained from the proposed method, it is observed that the reconstruction from proposed method using 60 projections even provides more accurate line profile than that of the reference image reconstructed with 180 projections. This is because the reference image contains streaking artifacts even if it is reconstructed using 180 projections.

In order to quantify the reconstruction accuracy of reconstruction and to evaluate the structural similarity between the reference image and the reconstructed image, the RMSE and SSIM values are calculated using (54) and (56) respectively for each of the reconstructions. The reconstruction from 180 projections is used as the reference image for the calculation. The SI values are also calculated using (55) to quantify the streaking artifacts present in the reconstruction. The original phantom is used as the reference image for calculating the SI because the reference reconstruction from 180 projections also contains streaking artifacts. The numerical values are given in Table 4.3 and a comparison among the values is presented in Figure 4.6 to evaluate the performance of the proposed algorithm. From visual inspection as shown in Figure 4.4 it can be decided that the streaking artifacts are insignificant for the normalized SI values lower than 0.6. From the qualitative comparison in Figure 4.4, the line profiles in Figure 4.5, and the plot of the quantitative values in Figure 4.6, it can be concluded that the proposed method can achieve improved results with quality reconstruction while more than 60 views are available.
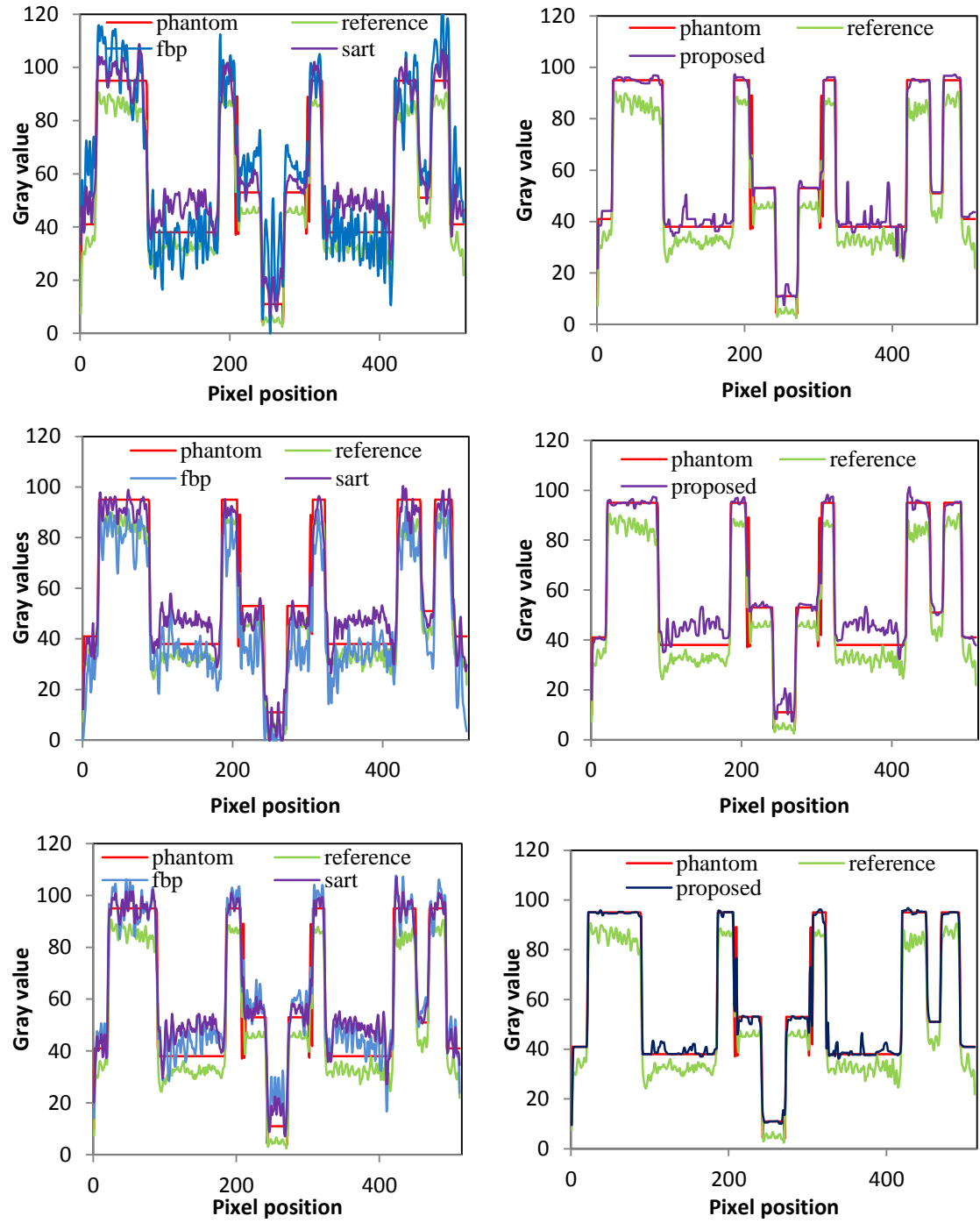
Figure 4.5. Line profile comparison of the noise-free phantom corresponding to the images in Figure 4.3 and Figure 4.4 along a line in the midplane of the fuel assembly phantom.

Table 4.3. Quantitative values of the reconstructions from noiseless projections

Views	Methods	RMSE	SI	SSIM
45	FBP	0.2203	3.1056	0.4739
	SART	0.1677	2.8704	0.7465
	Proposed Method	0.1663	2.4847	0.8064
60	FBP	0.1996	2.9381	0.5202
	SART	0.1659	1.9725	0.7526
	Proposed Method	0.1620	1.5887	0.8012
75	FBP	0.1809	2.6142	0.5855
	SART	0.1598	1.9604	0.7617
	Proposed Method	0.1574	1.5079	0.8070

4.3.1.2 Noisy-case. The principle of CS recovery is based on the assumptions that the signals are piecewise constant and noiseless. Thus, for the noisy measurements, exact recovery is not possible with the same number projections as the noiseless case. Experiments are conducted with Poisson noise added to the projections to validate the robustness of the proposed method. The images are reconstructed using the same number of projections and evaluated qualitatively and quantitatively similar to the noiseless case. The qualities of the reconstructed images are degraded due to the presence of noise as shown in Figure 4.7. The numerical values of the RMSE, SI, and SSIM values are given in Table 4.4.
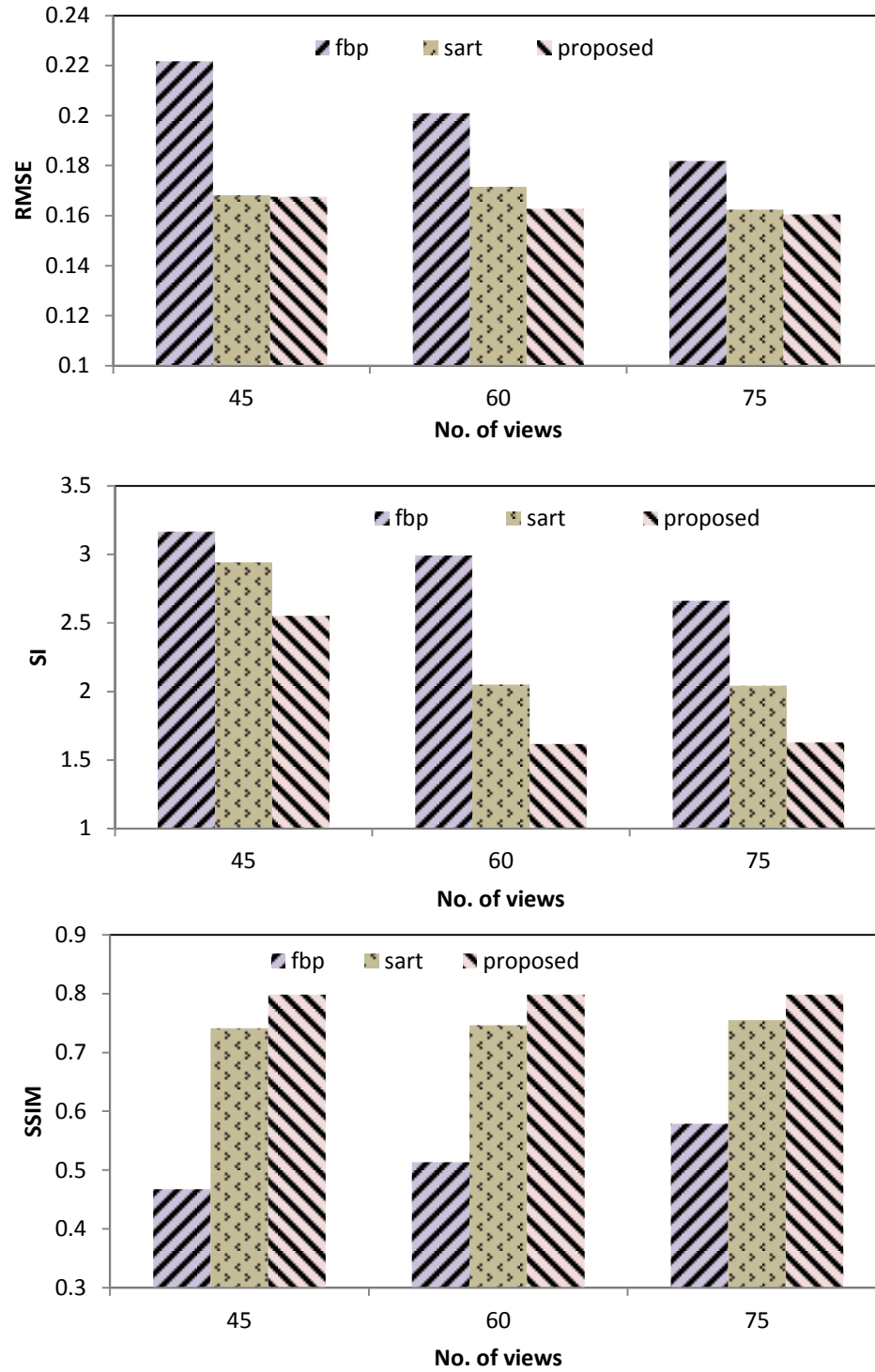
Figure 4.6. Plot of the quantitative values of the noise-free phantom with number of view angle and different algorithms.
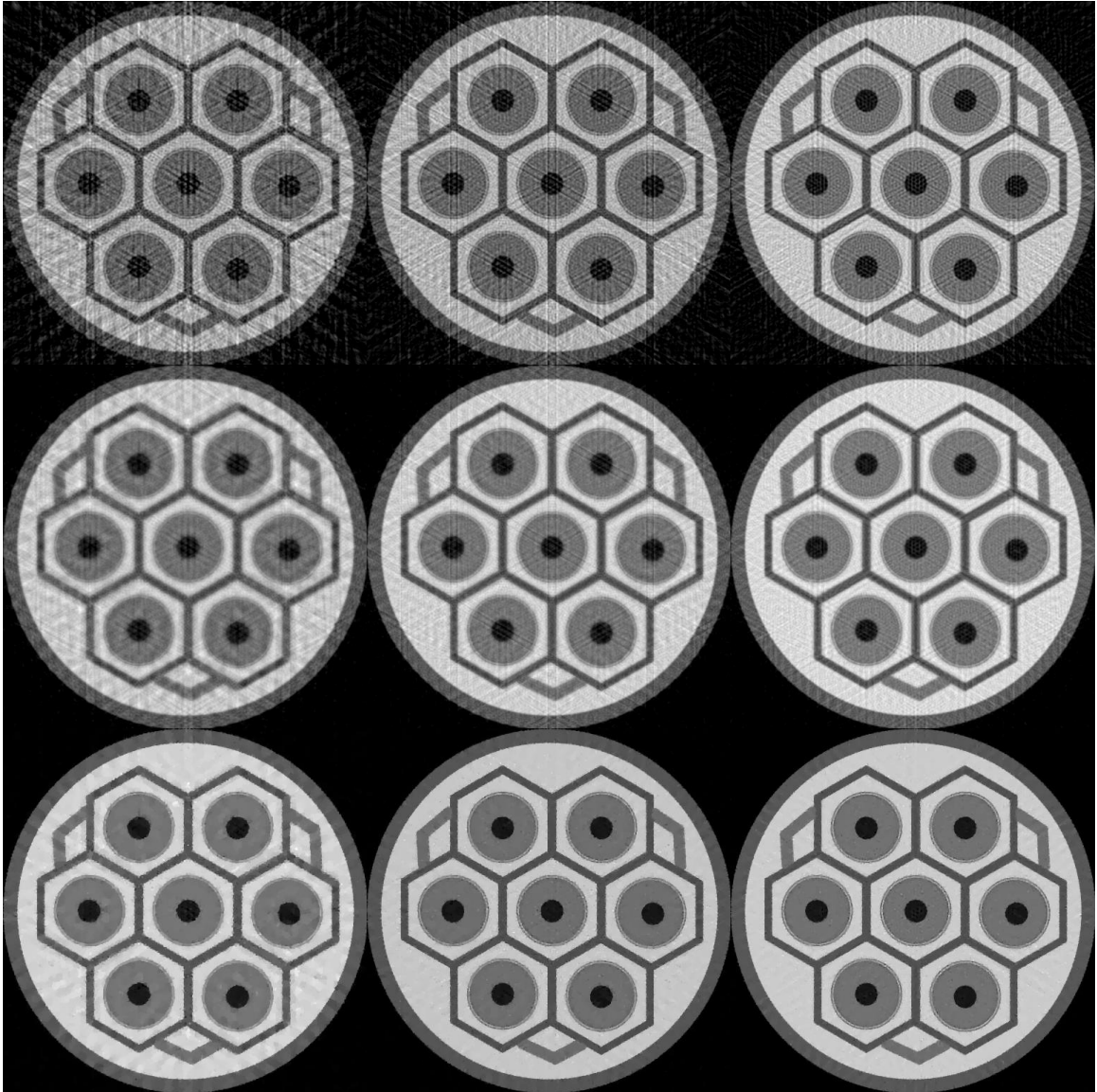
Figure 4.7. Reconstruction of noisy phantom using the FBP (first row), SART (second row), and TV based CS algorithms (third row) at three different view angles: 45 (first column), 60 (second column) and 75 (third column).

It is evident that, due to the presence of noise, the reconstruction accuracies are reduced, the streaking artifacts are increased, and the structural similarities are decreased. However, the proposed method provides better reconstruction than the FBP and the SART algorithm and the reconstruction quality and accuracy improves with the

increasing the number of projections. The line profiles in Figure 4.8 also validate that the line profile obtained from the proposed method is closer to the line profile of the original phantom.

Table 4.4. Quantitative values of the reconstructions from noisy projections

Views	Methods	RMSE	SI	SSIM
45	FBP	0.2217	3.1654	0.4674
	SART	0.1682	2.9415	0.7413
	Proposed Method	0.1676	2.5520	0.7981
60	FBP	0.2009	2.9922	0.5133
	SART	0.1715	2.0498	0.7464
	Proposed Method	0.1627	1.6143	0.7983
75	FBP	0.1819	2.6607	0.5790
	SART	0.1624	2.0408	0.7549
	Proposed Method	0.1605	1.6268	0.7981

4.3.2. Experimental Study. The proposed algorithm is validated through the reconstruction of the spent fuel assembly. The first, second, third, and fourth rows in Figure 4.9 shows the images reconstructed at four different axial location of the fuel
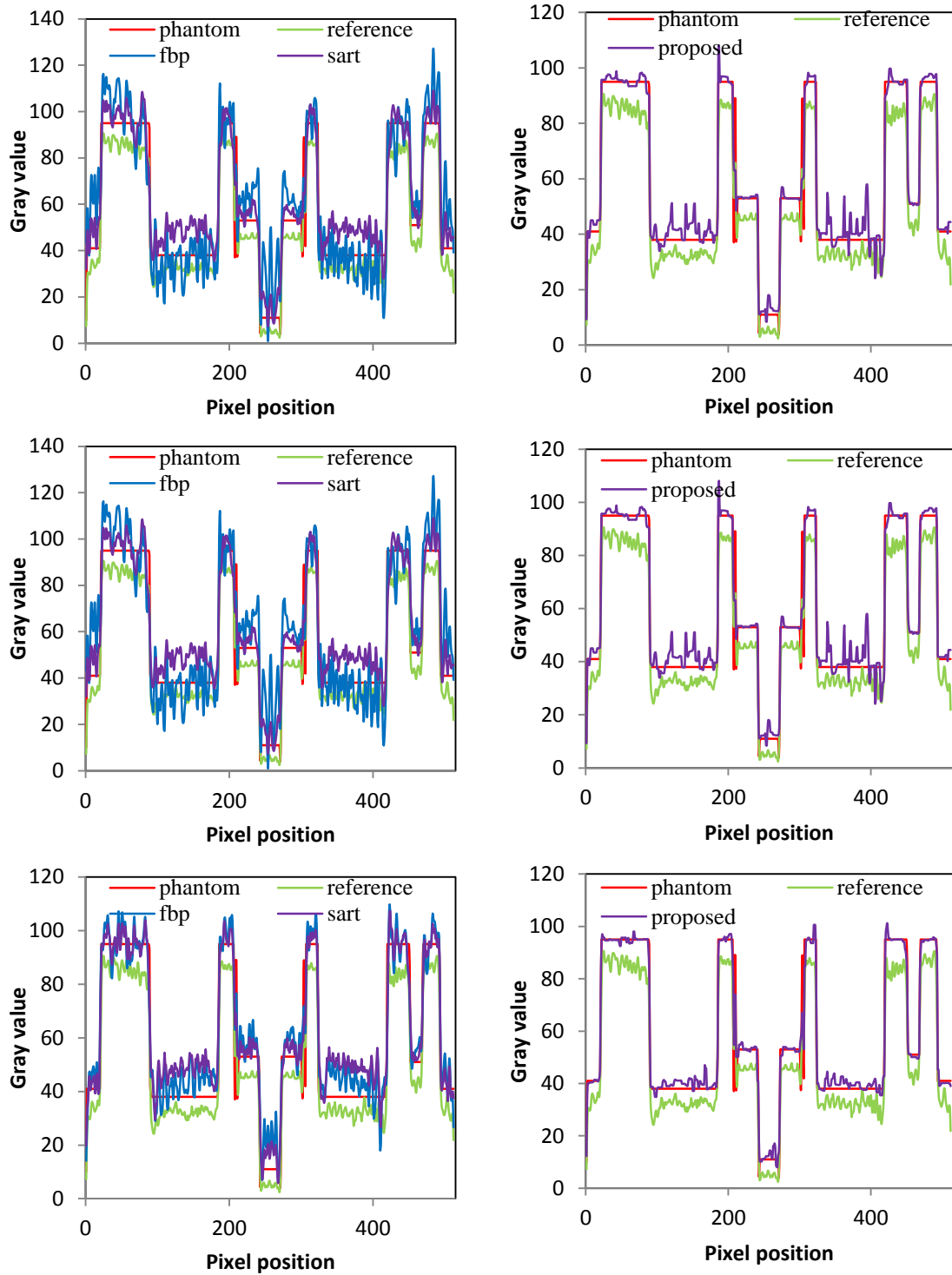
Figure 4.8. Line profile comparison corresponding to the images in Figure 4.3 and Figure 4.7 along a line in the midplane of the fuel assembly phantom at three different view angles: 45 (first row), 60 (second row) and 75 (third row).

assembly respectively. The reconstructions using FBP, SART, and proposed algorithm are shown in the first, second, and third column respectively. From the reconstructions, it is observed that severe artifacts exist in the FBP due to the limitation of the number of projections. SART provides better reconstruction compared to FBP, but the streak artifacts are still present. The proposed algorithm outperforms both methods yielding superior image quality in terms of artifact reduction and maintaining detail structures. It preserves most structural information without overshooting noise or any physical deformation. Since there is no reference image available, the reconstruction accuracy cannot be compared with the reference reconstruction.

To better understand the convergence speed of the proposed algorithms the regularization parameter λ, RMSE, and the SI values are plotted against the number of iterations. The regularization parameter is chosen automatically in each iteration according to the DP. The plots in Figure 4.12 show that the λ value decreases drastically within 4 iterations. The RMSE and the SI values also decrease dramatically that indicates the high convergence of the proposed algorithm. From the plots it is obvious that after about 50 iterations the convergence rate is almost stable, therefore 50 iterations are sufficient for this experiment.

The reconstruction of the spent fuel assembly was performed from all axial positions using the proposed algorithm. A 3-dimensional representation of several series of slices is shown in Figure 4.11. The AVIZO software is used to generate the 3D representation.
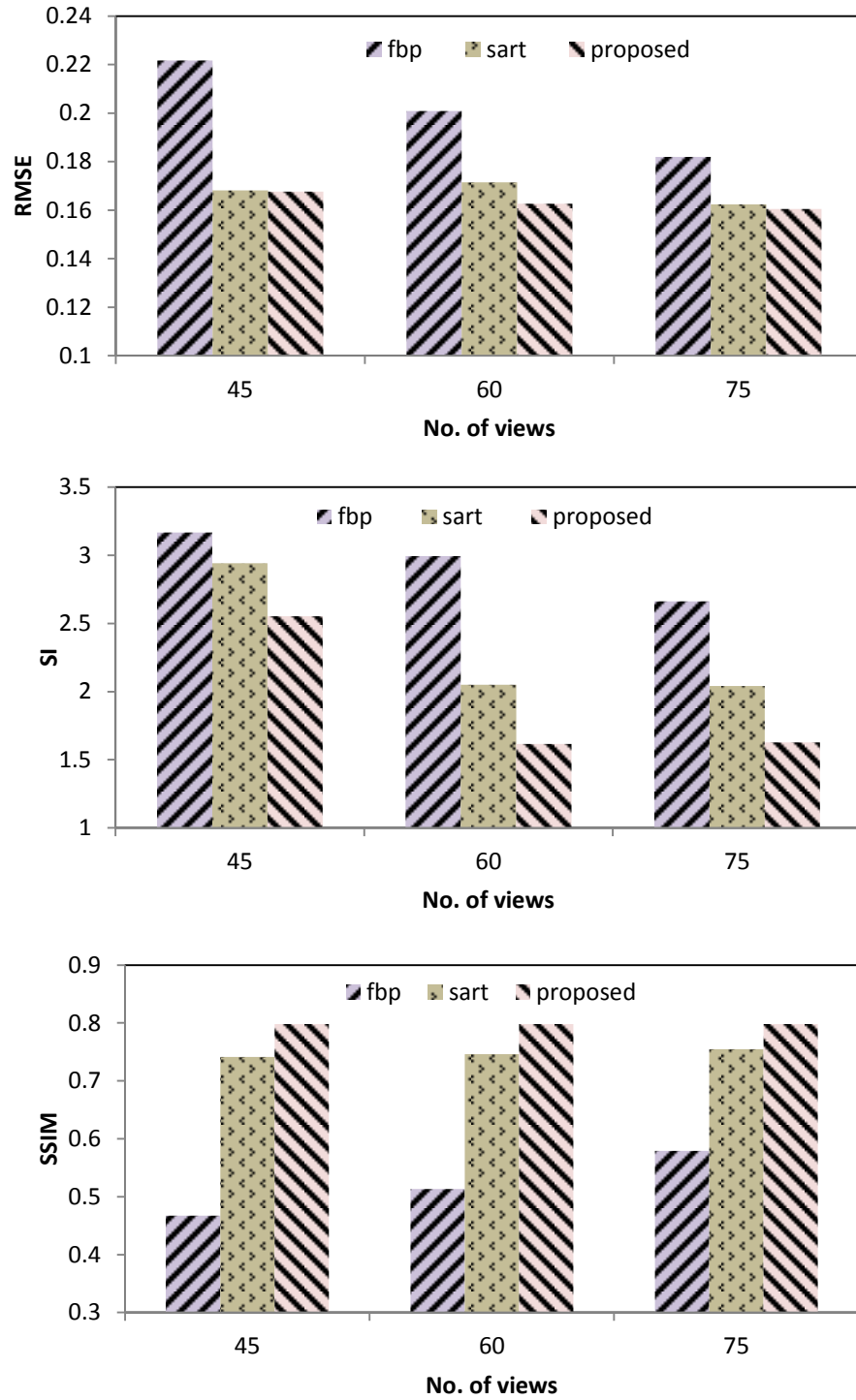
Figure 4.9. Plot of the quantitative values of the noisy phantom with number of view angle and different algorithms.
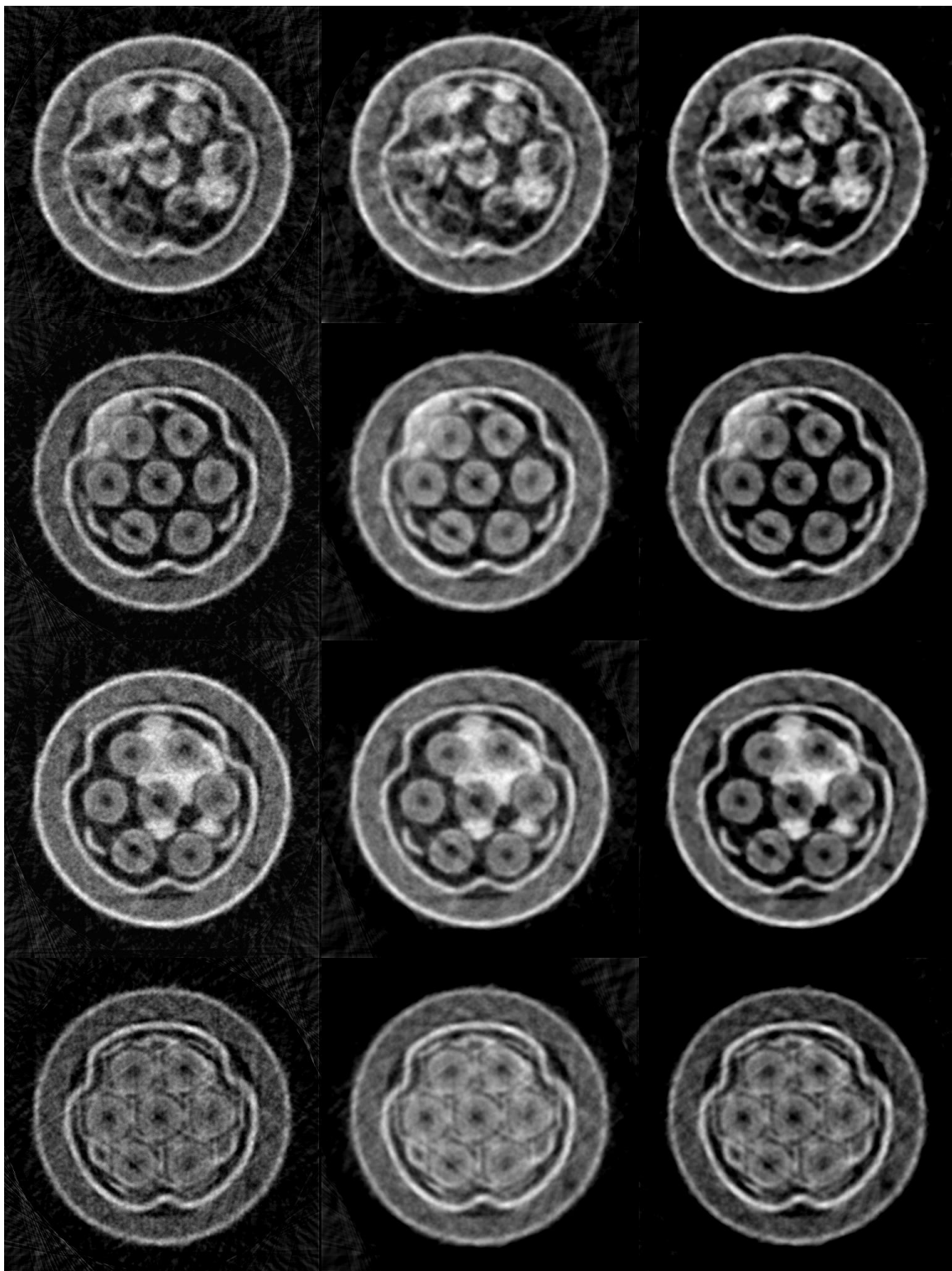
Figure 4.10. Reconstruction of the spent fuel assembly from 75 projections at four axial locations.
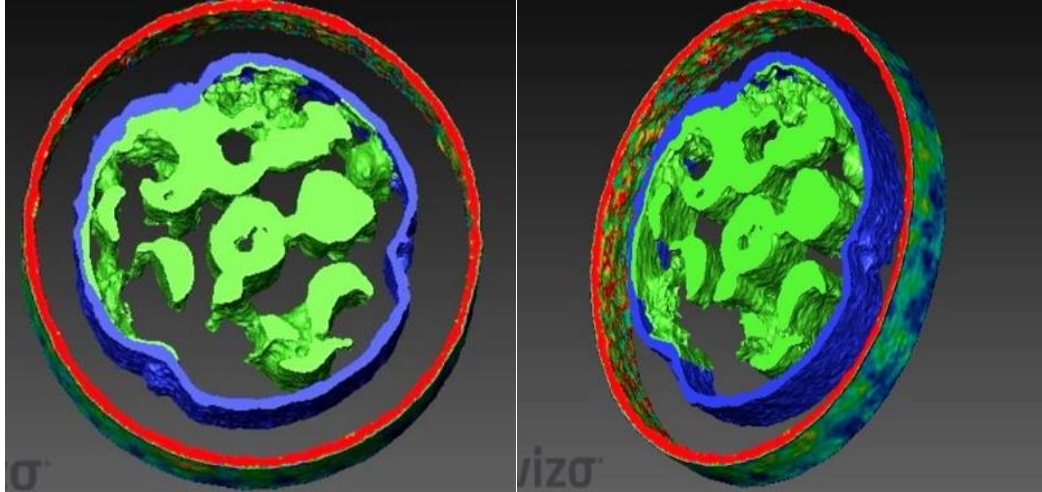
Figure 4.11. The three-dimensional reconstruction of the spent fuel assembly from two views.

4.4. DISCUSSION

CS inspired CT has been widely reviewed for the reconstruction of X-ray projection data on noisy and/or sparse-view measurements. In most cases, the underlying mathematics was formed based on additive white Gaussian noise. We implemented CS-based CT reconstruction method for neutron projection images assuming the projection images are contaminated by Poisson noise. The simulation and the experiments both indicate the usefulness of the TV based algorithm using few projection images in terms of reducing streaking artifacts and preserving fine structures. To the best our knowledge, no TV based method utilizing the ERP has been proposed for the tomographic reconstruction from the Poisson corrupted neutron projection images. We propose to use the Chambolle's dual approach for Poisson noise instead of using gradient descent proposed by Sidky et al [75] because it guarantees the convergence and solves the
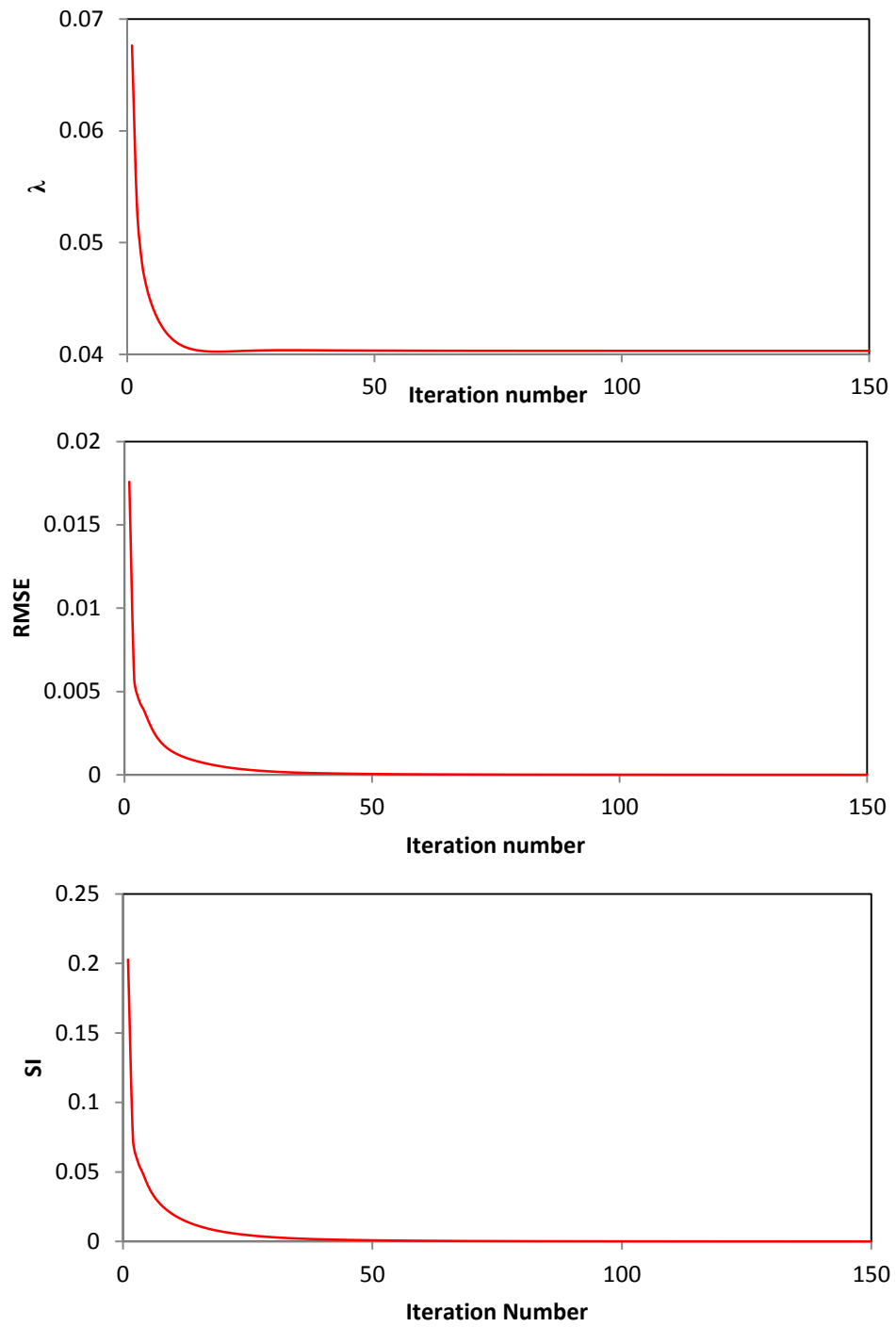
Figure 4.12. Plot of regularization parameter, RMSE, and SI for the experimental data.

minimization problem as a unconstrained minimization reconstruction to exactly solve it instead of approximation.

The simulation and experimental studies demonstrate that the proposed method provides better results than the classical reconstruction methods, resulting better image quality. The simulation study is evaluated with quantitative analysis to illustrate its accuracy and then applied to the neutron projection images for reconstruction. In both simulation and experimental study, the reconstructions display improved image quality.

Although TV methods proved to be superior in terms of reconstructing high-quality images, the major disadvantage of this method is that, the regularization of TV functional penalizes the image gradient irrespective to the information of the underlying structures, hence the loss of low contrast information (i.e. fine details) due to over-smoothing [83]. The number of iteration in the minimization is very important to generate a good quality reconstruction without over-smoothing.

The proposed method takes longer time than the conventional method, but the main purpose of this study is to achieve better reconstruction using few projections. The run time analysis was beyond the scope of this work. We implemented our proposed method in MATLAB R2013b. The computational time was longer than usual, but this can be handled by writing the code in visual C++ and using graphics processing unit (GPU).

5. RECONSTRUCTION OF AFIP-7 MOCKUP ASSEMBLY

5.1. INTRODUCTION

As mentioned earlier, the neutron tomography setup at the INL uses an indirect foil-film transfer technique for the irradiated object imaging. Therefore, it requires longer acquisition time, which prohibits acquiring a large number of projection images over 360˚ or 180˚. The AFIP-7 experiment seeks accurate reconstruction from very few projections to assess geometric stability of the U-Mo monolithic fuel assembly. The research presented here offers reconstruction strategies for the PIE of the AFIP-7 fuel assembly, based upon the recent established mathematical theory, compressed sensing (CS) that provides accurate reconstruction from highly undersampled data.

Image reconstructions from sparse projections are broadly discussed in Chapter 4. CS-based reconstruction algorithm was developed for reconstructing the spent fuel assembly with sparse projections. In this chapter, CS-based approach is used to reconstruct the AFIP-7 fuel assembly for both sparse and limited angle scan modalities. The reconstructions are obtained from a simulation and a mockup study to determine which procedure will provide superior reconstruction for the future AFIP-7 experiment.

The use of limited angle CT or tomosynthesis is common in many applications (e.g. dental CT [96], breast tomosynthesis [97] or straight line trajectory [98].) due to the large object size and restricted scanning In tomosynthesis, the projection images are acquired over a limited angular range instead of covering full 180˚ range (see Figure 1.5) and reconstructions are obtained using reconstruction algorithms. However, image quality from limited angle reconstruction for a specific number of views is different compared with the reconstruction from sparse-views because the spatial resolution in the

limited angle reconstructed image is highly anisotropic [4]. Decreasing the angular range of acquisition improves the resolution of the in-plane objects, but the spatial resolution of the out-of-plane structures decreases significantly [99]. From

Figure 5.1, it can be seen that the limited angular scan cannot cover the out-of-plane object from all three views, thus the out-of-plane structure cannot the reconstructed accurately. The extent of the angular range is also an important factor for the limited angle reconstruction. Wider angular range coves more voxel inside the object compared with the narrow angular range (see Figure 5.2). With the narrower angular range, the reconstruction will provide high-quality image near to the center of rotation but the length of the in-plane range will be reduced.
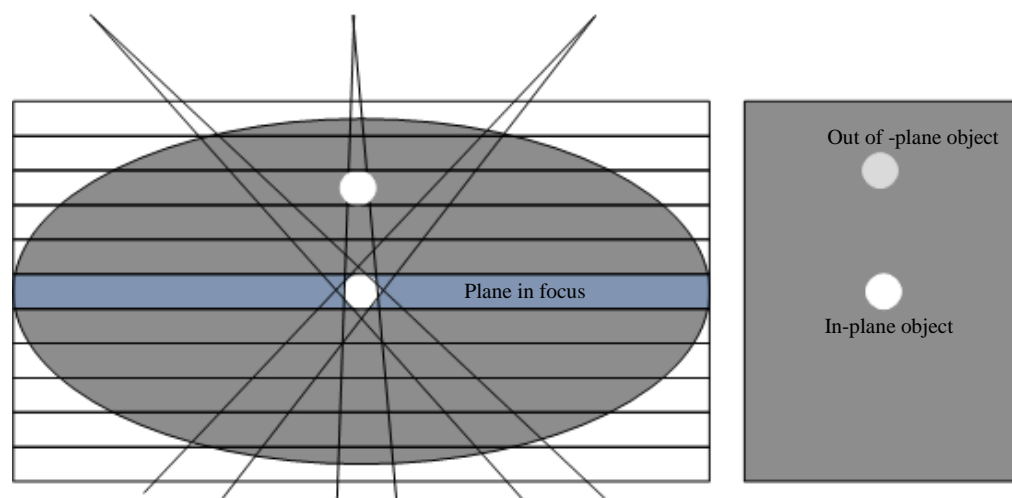
Figure 5.1. Illustration of the limited angle CT. It shows that the out-of-plane structure loses resolution.
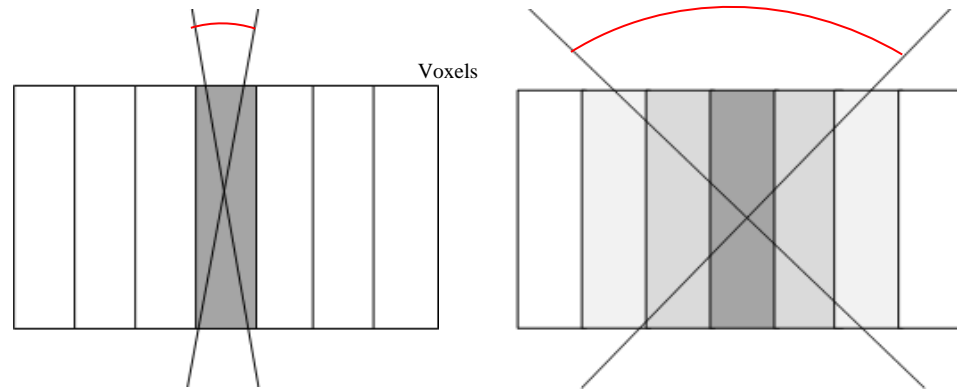
Figure 5.2. Backprojected rays shows that the wide angle covers more voxels than the narrow angle. The narrow angle reduces the length of the in-plane range.

Existing reconstruction algorithms for tomosynthesis are coarsely divided into four categories: simple backprojection, transfer algorithm such as filtered backprojection, algebraic reconstruction and the statistical image reconstruction method. In early tomosynthesis, the reconstruction process involved simply shifting and adding (SAA) the projections that was taken over the limited angular range. A certain plane inside the object of interest is focused and reconstructed while the out of focal planes were blurred. This method is also termed as simple backprojection. However, simple or filtered backprojection (FBP) algorithms generate out-of-plane artifacts during reconstruction, creating blurred versions of the in-plane objects. Several reconstruction methods are proposed to suppress or reduce the amplitude of out-of-plane artifacts [100-102].

However, CS-based methods are extensively studied for sparse-view CT reconstruction[3, 37, 45, 46, 48, 56-58, 80, 82]. Recently, CS- based reconstruction efforts have been made for the limited angle reconstruction. [96] [103]. In this work, several algorithms are selected and applied to the sparse-view and limited angle

representative data to investigate which method will provide accurate and artifact free reconstruction for the AFIP-7 experiment. The selected algorithms in this study include SAA or the simple backprojection (BP), FBP, and SART algorithm. A novel CS-based reconstruction algorithm is also proposed.

5.2. MATERIALS AND METHODS

As mentioned earlier, experiments using irradiated nuclear fuel have limited access and very expensive to conduct, therefore, it is impractical to perform any experiments without conducting simulations. A computer generated AFIP-7 fuel assembly phantom with actual geometries is generated and a mockup of the AFIP-7 fuel assembly made of aluminum is also fabricated at the INL and projection images are taken using X-rays. This study will justify the effectiveness of the sparse-view and limited angle CT to measure channel gaps accurately, providing accurate reconstruction. This study will also determine the optimal imaging parameters (i.e. the number of projections, angular range, and angular increment) for the actual AFIP-7 neutron tomography experiment. However, in order to find the accurate measurements using few number of projection images, reconstruction algorithms needs to be developed that will provide accurate reconstruction using few views.

The BP, FBP, and SART methods are already described in chapter 3. The proposed CS method will be described here. In the context of tomosynthesis, an anisotropic TV based image reconstruction algorithm is proposed. We solve the sparse-view problem using isotropic TV minimization as describe in Chapter 4. We implement

anisotropic TV minimization algorithm for the limited angle reconstruction problem. The anisotropic TV minimization algorithm solves the following optimization problem,

$$\mu_{k+1}^* = \underset{\mu}{minimize} \left\{ \frac{1}{2} \int_\Omega \frac{(\mu^* - \mu_{k+\frac{1}{2}}^*)^2}{\mu_k^*} + \lambda \|\mu^*\|_{ATV} + \|\mu^*\|_{USM} \right\} \qquad (66)$$

The motivation of using anisotropic TV is that it gives the privilege to reconstruct images in a particular edge direction [104]. As shown in Figure 2.5, in case of limited angle problem, there are limited sampling points in the Fourier space along v-axis. Therefore, the projections cannot record any edge information in that direction. Thus, the energy vacancy in that direction would be filled by artifacts. The reconstructed image contain different resolution along each axis, thus weighing the TV term can produce better reconstruction compared to isotropic reconstruction [87]. Using ATV, the TV term will be weighted and the artifacts and blurring would be suppressed by assigning more energy in the horizontal axis compared to the vertical axis.

Iterative reconstruction using TV minimization can significantly reduce noise and streak artifacts in CT images compared to the classical reconstruction algorithms, however, TV minimization process is prone to over-smoothing sharp anatomical structures. Therefore, we incorporate a sharpening tool with the TV minimization process to retain sharp boundaries. The sharpening process is performed to the TV minimized image using unsharp masking. The unsharp masking process simultaneously enhance contrast and sharpness as well as reduces halo effect that is generated by means of edge-preserving TV minimization [105].

Table 5.1. Implementation steps of the proposed method

Proposed Algorithm

Input: β ; **Initialization:** $u^0 = 0$

//SART step

while $\left|RMSE^j - RMSE^{j-1}\right| < 10^{-5}$

$\quad u^j = SART\ (u^{j-1})$

end $\quad u^{SART} = u^j$

//positivity constraint

$\quad$ **if**

$\quad\quad\quad u^{SART} < 0$

$\quad\quad\quad u^{SART} = 0$

$\quad$ **end**

// ATV minimization

$v^0 = u^{SART}, b^0 = d^0 = 0, \lambda > 0, \mu > 0, \varepsilon, tol$

while $\varepsilon > tol$

$\quad v^{k+1} = (CG)^k$

$\quad d^{k+1} = \text{shrink}(\nabla v^{k+1} + b^k, \mu/\lambda)$

$\quad b^{k+1} = \text{shrink}(\nabla v^{k+1} - d^{k+1}, \mu/\lambda)$

end

$u^{Opt} = v^{k+1}$

$u^{Out} = USM(u^{Opt})$

5.3. RESULTS

This section presents the numerical results from simulated and the experimented data to validate and evaluate the reconstruction algorithms. The study includes the influence of different angular ranges and angular spacing in both sparse-view CT and tomosynthesis. The quantitative analysis of the reconstruction methods is assessed to evaluate the reconstruction methods.

5.3.1. Simulation Study. The phantom study was assumed to be parallel beam geometry since neutron imaging also assumes parallel beam configuration. The simulated phantom consists of AFIP-7 fuel foil sandwiched in aluminum clad as seen in Figure 5.3. Since aluminum is almost transparent to neutron, it cannot produce visible contrast while projection images are taken. Therefore, the projection images of AFIP-7 fuel assembly will contain the information about the fuel foil only. Figure 5.4 shows three projection images of the fuel assembly from three different angular positions.

From visual inspection, it is prominent that the proposed CS based ATV minimization method provides significant image quality compared to the classical reconstruction methods in both sparse-view and limited angle reconstruction. The edges are sharpened and the results are very close to the original phantom in contrast to the other methods as well as the streak artifacts is significantly reduced. The most determinative factor of the limited angle problem is the angular range. In this experiment, $\pm 18°$, $\pm 22°$, $\pm 30°$, $\pm 45°$, and $\pm 90°$ angular ranges are taken with an increment of $1°$ considering $0°$ position parallel to the plates as shown in Figure 5.3. The $\pm 90°$ angular range also refers as the conventional CT acquisition process. Since many factors affect the image reconstruction in real experiment, such as beam-hardening, scattering, focal-

spot size, etc., Poisson noise is added to simulate realistic measurement and evaluate the stability of the proposed algorithm. For the sparse view problem, we consider the same number of projection images as limited angular case considering 1°, 2°, 3°, 4°, and 5° increment covering 180° angular range.
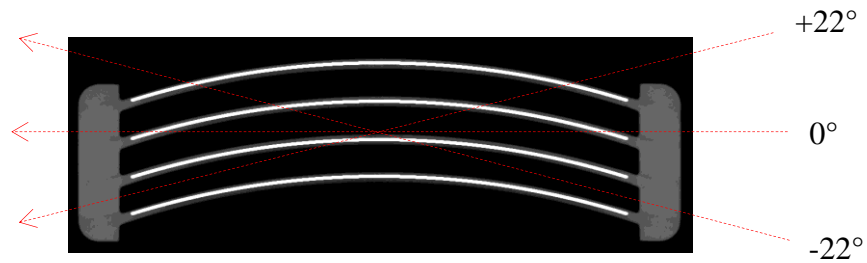

Figure 5.3. Diagram showing the projection acquisition direction for AFIP-7 fuel assembly.
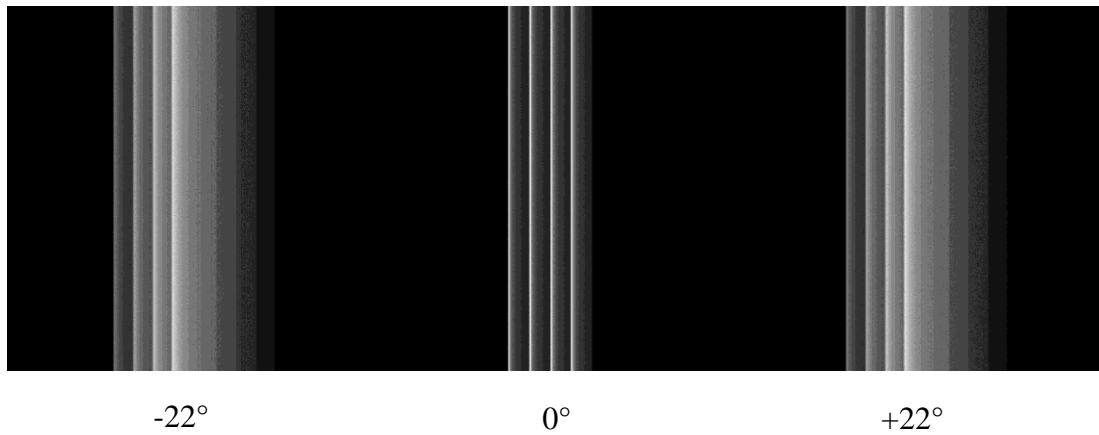

Figure 5.4. Example of projection images simulated at three different angular positions.

The reconstruction of the phantom using different reconstruction methods for both limited angle and sparse-view case are shown in Figure 5.6 and Figure 5.7 respectively. In each figure, results on first, second, third, and fourth row are reconstructed by BP, FBP, SART, and proposed method accordingly. To make the results visually comparable, each column shows the reconstruction of different angular views. Comparing the reconstructed image quality visually and by quantitative analysis, it can be seen that, the reconstruction using limited angle provides better reconstruction with geometric stability and less artifacts.

5.3.2. Experimental Study. The experimental mockup study uses cone beam geometry and the projection images were obtained at the INL imaging facility using a Varian PaxScan CP2-Lite X-ray imager with detector resolution of .127mm×.127mm in size. The source to detector distance was set as 466.725mm and source to object distance was 225.425mm. The projection images obtained had 1536×1920 pixels in size. 1441 projection images were obtained covering 360° with an angular increment of 0.25°. The raw images are normalized using a simple mathematical process to clean up the data due to imperfection of the incident beam. The normalization is performed using an open beam image and a dark image. In order to match the intensity of the open beam with the raw projection image, several regions of interest are chosen from the background regions and average intensities are calculated from both open beam data and the raw data. The average of the ratio of the intensities provides the correction factor to apply to the projection images. The dark image was also acquired while the beam is turned off. It corrects the electronic noise. The mathematical formula for normalization is,

$$ND = \frac{Raw\ data - Dark\ image}{Open\ beam - Dark\ image} \tag{67}$$

The raw projection images were also pre-processed using alpha trimmed mean filter [106] to correct defective pixels. The data are reduced by equally skipping the full data set. The angular range and angular increment of the projection images are same as chosen for phantom study and the acquisition geometry is also similar to Figure 5.3.

For the limited angle case (see Figure 5.8), the reconstruction using BP, FBP, and SART shows sequential improvement compared to each other. Among them, the FBP reconstruction shows high spatial frequency noise over the entire area due to limited sampling rate. Reconstruction using BP enhances low frequency information, thus produces blurred reconstruction. The SART reconstruction improves the reconstruction by reducing the streak artifacts and noise, but the residual artifacts can still be seen. Besides, SART suffers from edge blurring artifacts and low contrast features are lost. The reconstruction from the proposed method produces better reconstruction than the BP, FBP and SART reconstruction. Streak artifacts are less visible than the other methods and the edges are much cleaner and sharper. The reconstruction accuracy is further justified with the quantitative analysis of the reconstruction methods. The quantitative evaluation parameters include the RMSE, SI, and SSIM as described in Section 3.4. The results indicate that the proposed method can achieve the highest reconstruction accuracy compared to the classical methods. The low SI value indicates that the proposed method can significantly suppress the streaking artifacts and noise which leads to an image of acceptable quality in the limited angular case.
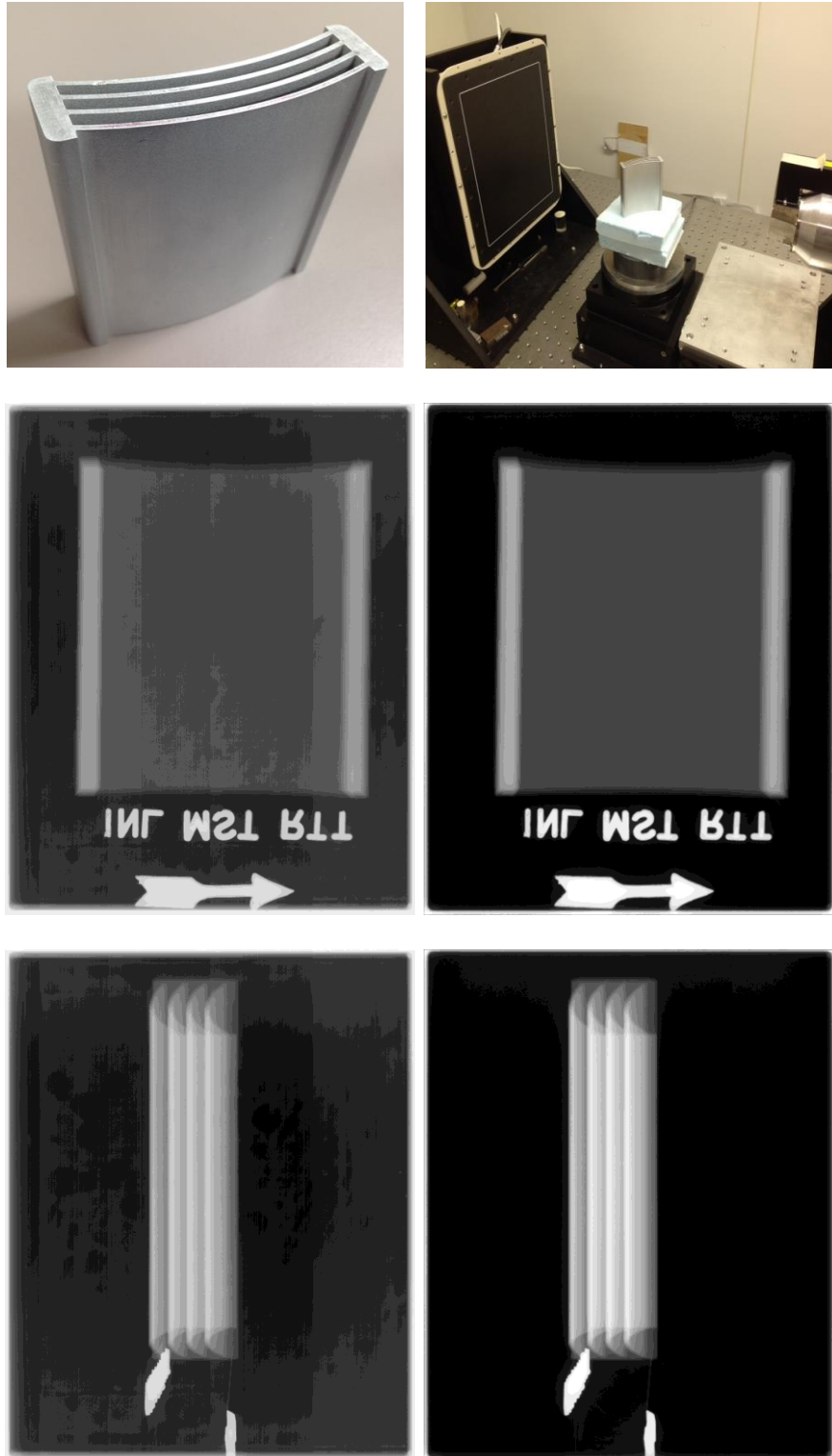
Figure 5.5. The top left image shows the AFIP-7 fuel assembly mockup, the top right image shows the setup of the image acquisition process, the middle and bottom left images are two raw projection images at two different angular views, the middle and bottom right images are the pre-processed images.

Compared to the sparse-view reconstruction (see Figure 5.10) of the fuel mockup assembly, the limited angle reconstruction provides better image quality, even with the isotropic/anisotropic TV minimization method. This is because the increasing angular spacing among the projection images creates strong artifacts due to the nature of the fuel assembly. The fuel assembly doesn't have a closed circular boundary, hence, the limited angle reconstruction can provide better reconstruction compared to the sparse-view reconstruction since it has the minimum angular spacing of 1°. For example, the spent fuel assembly in chapter 4 has closed circular boundary, thus reconstructing using limited angle will be very challenging for them. The resulting sparse-view reconstruction provides over-smoothing of the artifacts and the reconstructed image contains some blocky effects, especially when the number of projections images is less than 60. The reconstructed results from BP, FBP, SART, and the proposed method for both limited angle and sparse-view case are shown in Figure 5.8 and Figure 5.10 respectively to compare the reconstructed methods. The BP and FBP suffer from serious streak artifacts due to the limitation of the number of projections even with more projection views. SART improves the reconstructed result but still contains artifacts. The proposed method reduces the artifacts significantly specially with 45 or more projection images. Although the artifacts are reduced in the reconstructed image but due to the lack of sufficient projection images, the artifacts cause geometric instability, produces blocky artifacts and detail features become blurred.
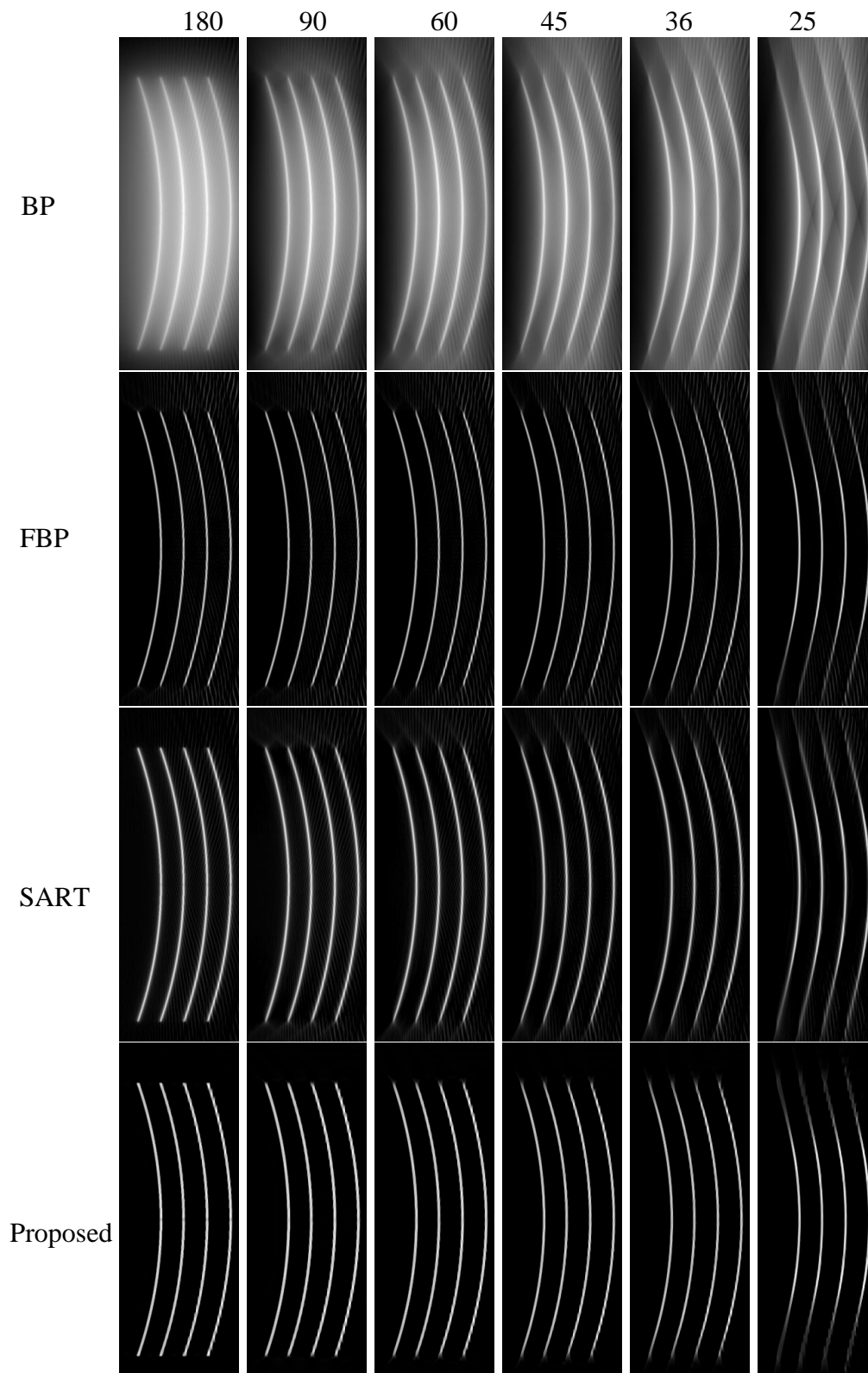
Figure 5.6. Limited angle reconstruction of the AFIP-7 fuel assembly phantom with 180, 90, 45, 36, and 25 projections with uniform sampling of 1° increment using (a) BP, (b) FBP, (c) SART, and (d) proposed method.

Figure 5.7. Sparse-view reconstruction of the AFIP-7 fuel assembly phantom with181, 91, 61, 45, and 37 projections with uniform sampling of 180° angular range using (a) BP, (b) FBP, (c) SART, and (d) proposed method.

Figure 5.8. Limited angle reconstruction of the AFIP-7 fuel assembly mockup
with181, 91, 61, 45, 37, and 25 projections with uniform sampling of 1° increment
using (a) BP, (b) FBP, (c) SART, and (d) proposed method.

Figure 5.9. Quantitative evaluation of the limited angle reconstruction of AFIP-7 fuel assembly mockup.
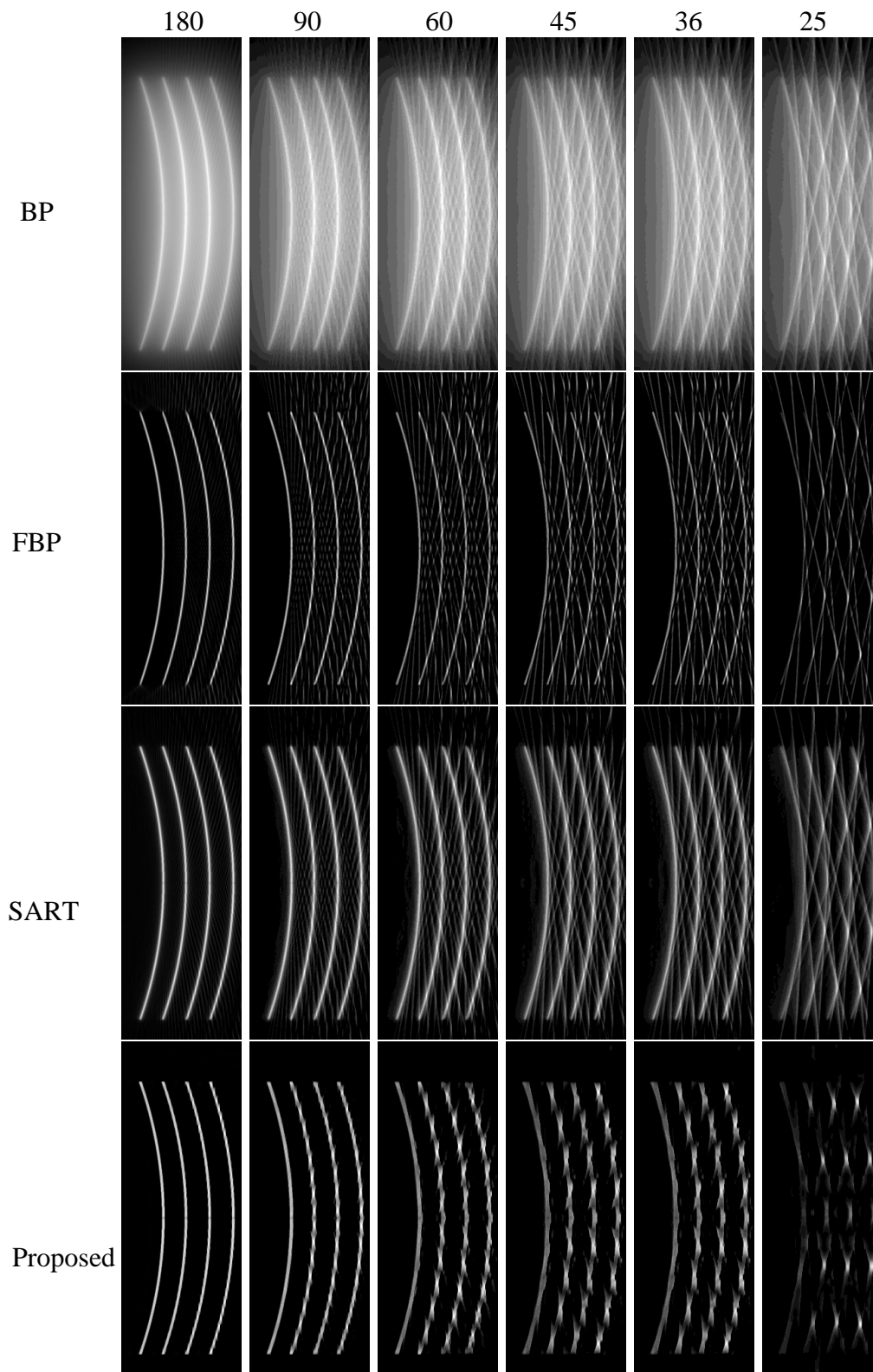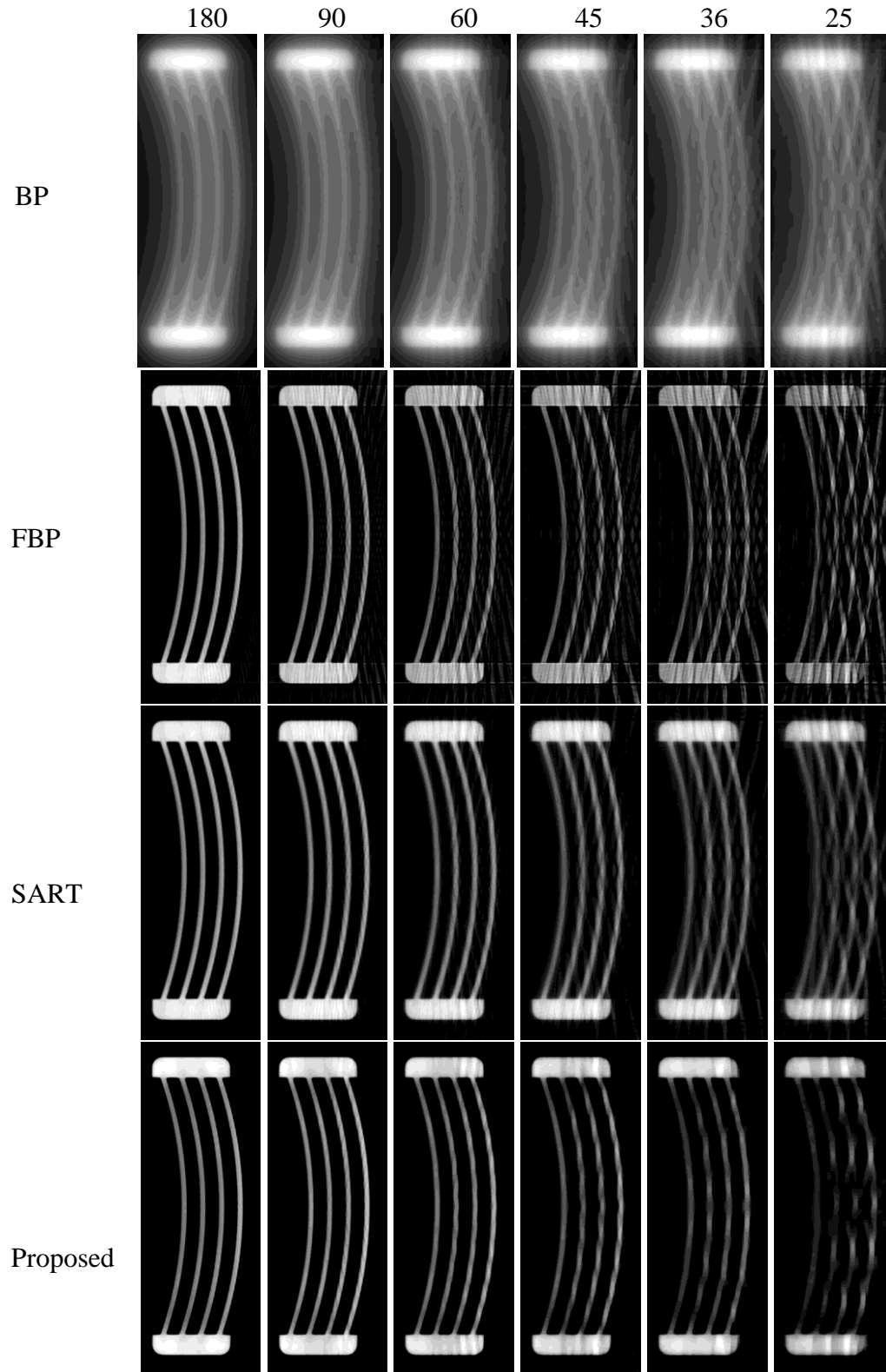
Figure 5.10. Sparse-view reconstruction of the AFIP-7 fuel assembly mockup with180, 90, 60, 45, 36, and 25 projections with uniform sampling of 180° angular range using (a) BP, (b) FBP, (c) SART, and (d) proposed method.
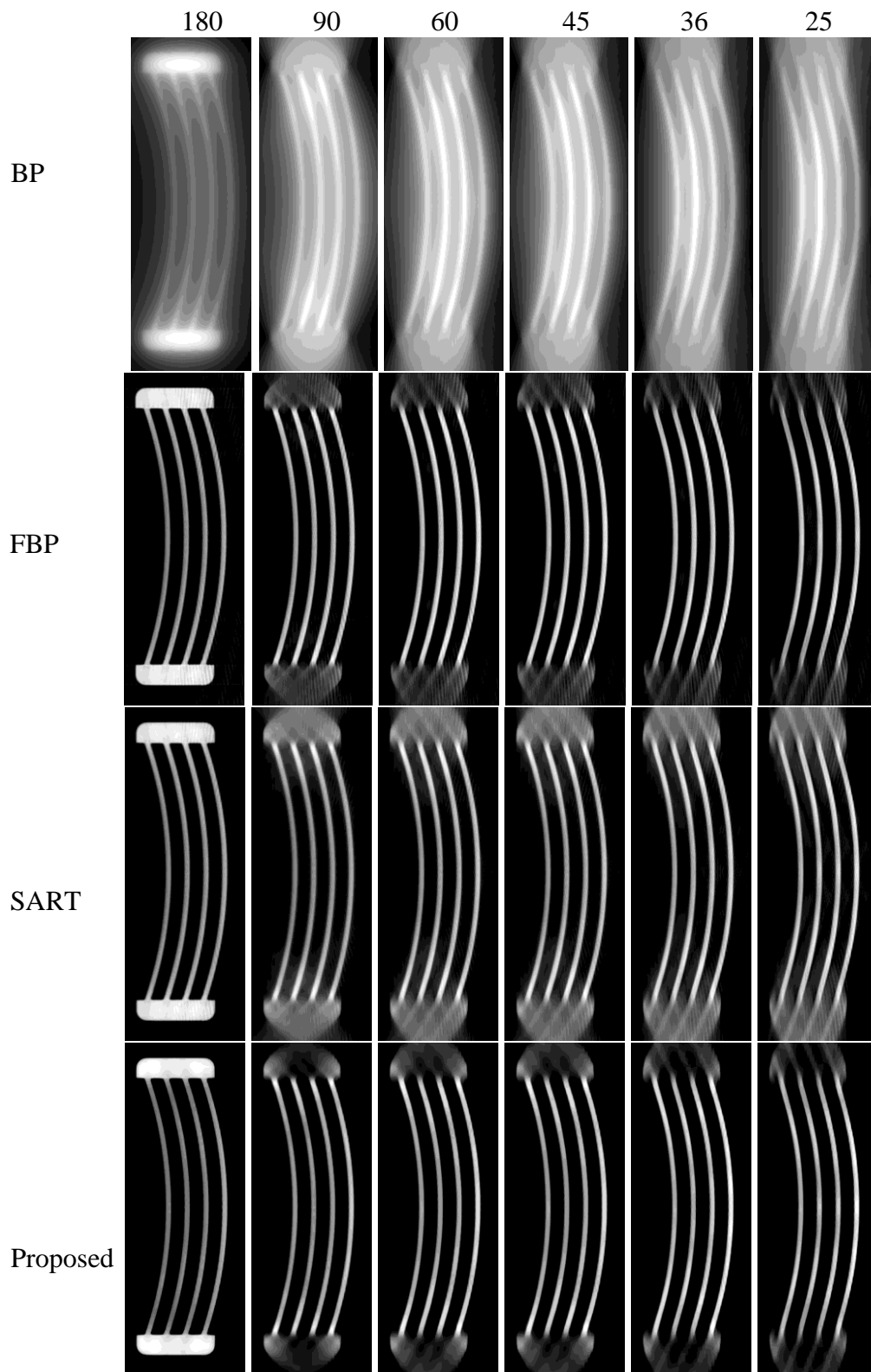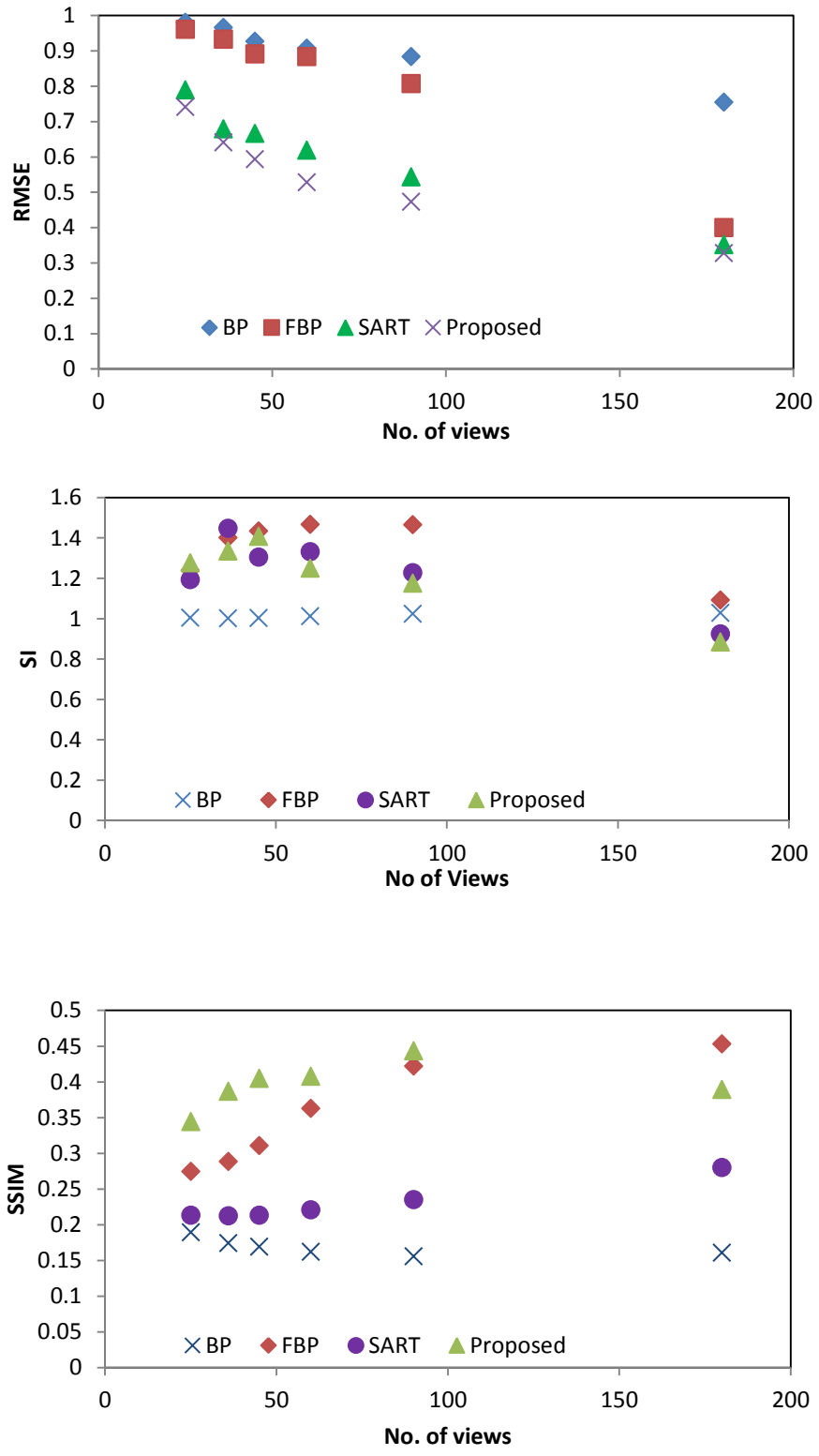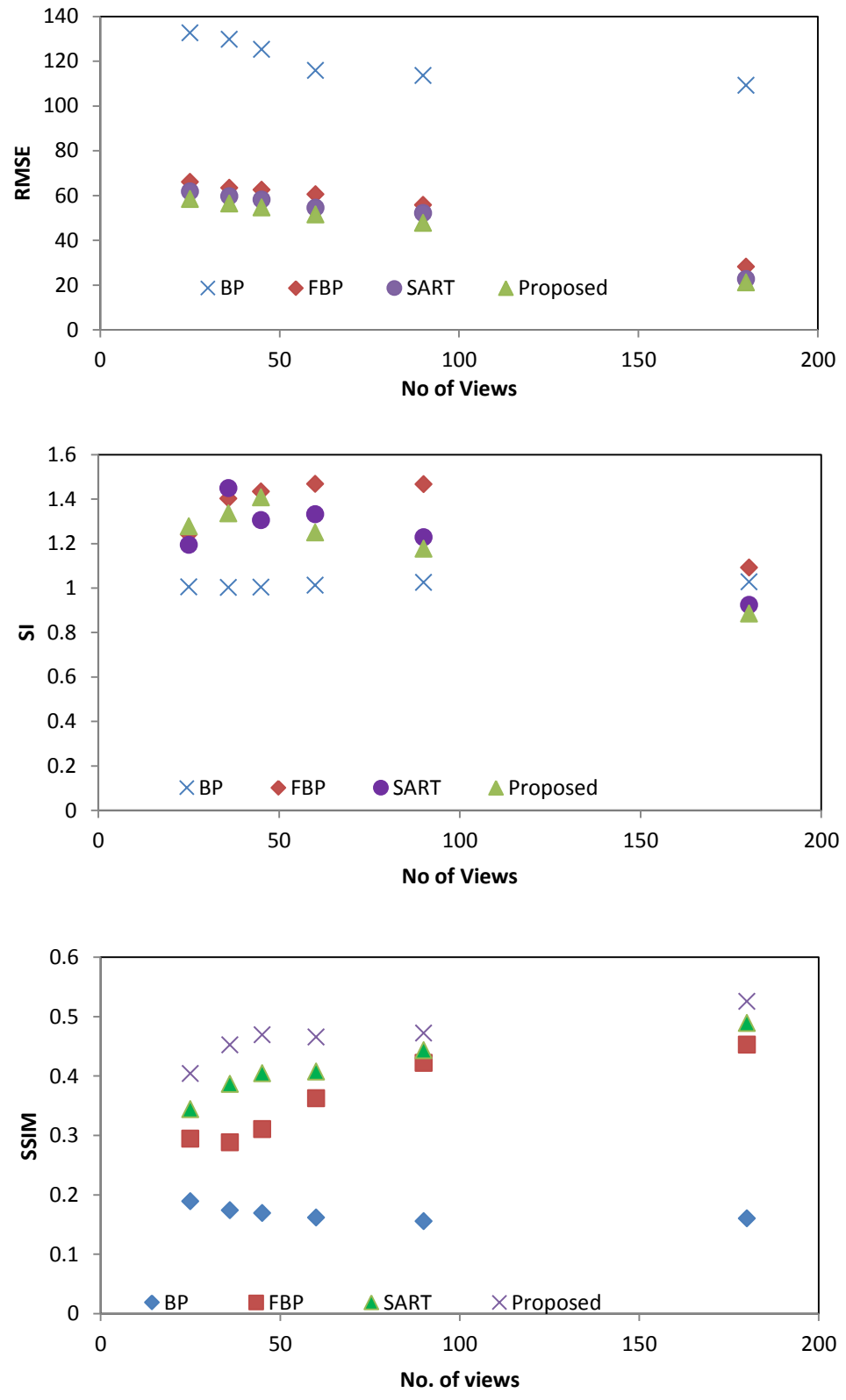
Figure 5.11. Quantitative evaluation of the sparse-view reconstruction of AFIP-7 fuel assembly mockup.

5.4. DISCUSSION

The reconstruction results of both sparse-view and limited angle reconstruction suggest that the limited angle geometry is more suitable for the accurate reconstruction of the AFIP-7 fuel assembly experiment. Reconstruction results suggest that accurate reconstruction can be obtained using limited angle geometry if 36 or more projection can be acquired with an angular spacing of 1°. However, as seen from the reconstructed images, the limited angle reconstruction cannot provide accurate reconstruction of the end fittings in the limited angular case. Since the purpose of the AFIP-7 experiment is to find the coolant channel gap accurately; reconstruction of the end fittings is not the main purpose of this experiment.

Limited angle reconstruction can reconstruct the coolant channel gap accurately. Sparse-view reconstruction can provide the channel gaps together with the end fittings but the overall image quality degrades while the number of projection images fall below 60. However, several factors should be taken into account for the actual AFIP-7 experiment, such as the geometric distortion of the AFIP-7 fuel under irradiation can change the gross structure of the fuel foil, thus changes the actual shape of the fuel foil assembly. Another important factor is the spatial resolution of the film. The experiment will use the film based acquisition, therefore the resolution and contrast of the film based projection image will be different compared to the X-ray projection images. These factors will also affect the reconstruction quality which can be improved by increasing the number of projection images.

6. SUMMARY AND CONCLUSION

The research presented here focuses on the capability spent or irradiated nuclear fuel assembly inspection using neutron tomography. The scientific goal is to achieve quality reconstruction possible from very few neutron projection images. The reconstruction assesses geometric integrity of the nuclear fuel assemblies. The purpose centers on providing supplemental cost-efficient non-destructive post-irradiation examination of the nuclear fuel assemblies and safeguards improvements affiliated with nuclear fuel storage and processing.

Due to potential high costs and difficulties with experiments involving computed tomography research using actual neutron projection images, simulations as well as previous measurements are utilized to establish confidence before conducting experiments. Simulations are useful to evaluate the proposed reconstruction strategies because it doesn't contain any unknown factors. The simulations include detailed representation of the physical configurations of the assembly components. Statistical distributions added to simulations provide ideas about the real measurements.

The experimental measurements with the spent fuel assembly serve as a benchmark for the safety improvements of nuclear power plants and reprocessing facilities. Reconstruction results confirm that neutron computed tomography can be used to examine the spent fuel assembly for identifying anomalies, such as any missing components or channel blockage due to fuel damage. The ability to identify anomalies in the assemblies permits early detection of fuel meltdowns as well as improves reprocessing facility operations.

The need for supplemental methods for the non-destructive PIE of the AFIP-7

experiment also drives to inspect the irradiated fuel assemblies using neutron tomography. Although experiments are yet to be conducted, the mockup study through simulations as well as experimental measurements through X-ray provides a good agreement for the future neutron PIE of the AFIP-7 assembly. The reconstruction results and analyses show that limited angle tomography is suitable for the AFIP-7 experiment compared with the sparse angle tomography. The optimal image acquisition parameters (angular range and the angular spacing) for obtaining neutron projection images of the AFIP-7 fuel assembly are recommended for best reconstruction and analysis using both modalities. However, there are several parameters that could shift the optimal parameters, such as the quality of neutron projection images. The amount of blurring and image artifact are also important factor for optimal image quality. However, the proposed reconstruction strategies improve image quality, reducing the amount of blurring and artifacts.

REFERENCES

[1]   Korea Atomic Energy Research Institute, http://www.kaeri.re.kr:8080/english/ sub/sub03_02_01_02.jsp 2015. (Accessed April 3, 2015)

[2]   G.S., C., *Comparison of HEU and LEU Neutron Spectrum for ATR Fuel Element and ATR Flux-Trap Positions*. October 2008, Idaho National Laboratory

[3]   Kudo, H., T. Suzuki, and E. A. Rashed, "Image reconstruction for sparse-view CT and interior CT—introduction to compressed sensing and differentiated backprojection," *Quantitative Imaging in Medicine and Surgery,* 2013. Vol. 3 (3): pp. 147-161.

[4]   Sechopoulos, I., "A review of breast tomosynthesis. Part I. The image acquisition process," *Medical Physics,* 2013. Vol. 40 (1): pp. 014301.

[5]   Sechopoulos, I., "A review of breast tomosynthesis. Part II. Image reconstruction, processing and analysis, and advanced applications," *Medical Physics,* 2013. Vol. 40 (1): pp. 014302.

[6]   Radon, J., "ON THE DETERMINATION OF FUNCTIONS FROM THEIR INTEGRAL VALUES ALONG CERTAIN MANIFOLDS," *IEEE Transactions on Medical Imaging,* 1986. Vol. MI-5 (4): pp. 170-176.

[7]   The official website of the nobel prize, 2014. (Accessed December 25, 2014)

[8]   Kak, A. C. and S. M., "*Principles of Computerized Tomographic Imaging*. 2001: Society for Industrial and Applied Mathematics.

[9]   Hopkins F. , D. Y., Lasyuk B. , Abraham A. , Basu S., "Analytical corrections for beam-hardening and object scatter in volumetric computed tomography systems," *In WCNDT,* 2004. Vol. 22: pp. 462–468.

[10]   Herman, G. T., "Correction for beam hardening in computed tomography," *Physics in Medicine and Biology,* 1979. Vol. 24 (1): pp. 81.

[11]   Brooks, R. A. and G. Di Chiro, "Beam hardening in X ray reconstructive tomography," *Physics in Medicine and Biology,* 1976. Vol. 21 (3): pp. 390-398.

[12]   Joseph, P. M. and R. D. Spital, "A method for correcting bone induced artifacts in computed tomography scanners," *Journal of Computer Assisted Tomography,* 1978. Vol. 2 (1): pp. 100-108.

[13]   Buzug, T., "*Computed tomography: From photon statistics to modern cone-beam CT*. 2008: Springer-Verlag Berlin Heidelberg.

[14] Beister, M., D. Kolditz, and W. A. Kalender, "Iterative reconstruction methods in X-ray CT," *Physica Medica,* 2012. Vol. 28 (2): pp. 94-108.

[15] Brooks R. A., D. G., "Principles of computer assisted tomogrphy (CAT) in radiographic and radioscopic imaging," *Physics in Medicine and Biology,* 1976. Vol. 21: pp. 689-732.

[16] Hounsfield, G. N., "Computerized transverse axial scanning (tomography): I. Description of system," *British Journal of Radiology,* 1973. Vol. 46 (552): pp. 1016-1022.

[17] Hsieh, J., et al., "Recent Advances in CT Image Reconstruction," *Current Radiology Reports,* 2013. Vol. 1 (1): pp. 39-51.

[18] Guan, H. and R. Gordon, "Computed tomography using algebraic reconstruction techniques (ARTs) with different projection access schemes: A comparison study under practical situations," *Physics in Medicine and Biology,* 1996. Vol. 41 (9): pp. 1727-1743.

[19] Hounsfield, G. N., *A method of and apparatus for examination of a body by radiation such as x or gamma radiation*, T.P. Office, Editor. 1972: London, UK.

[20] Kaczmarz, S., "Angenäherte Auflösung von Systemen linearer Gleichungen," *Bulletin of the International Academy of Polish Science and Letters A,* 1937: pp. 355-357.

[21] Jiang, M. and G. Wang, "Convergence studies on iterative algorithms for image reconstruction," *IEEE Transactions on Medical Imaging,* 2003. Vol. 22 (5): pp. 569-579.

[22] Hudson, H. M. and R. S. Larkin, "Accelerated image reconstruction using ordered subsets of projection data," *IEEE Transactions on Medical Imaging,* 1994. Vol. 13 (4): pp. 601-609.

[23] Xu, F., et al., "On the efficiency of iterative ordered subset reconstruction algorithms for acceleration on GPUs," *Computer Methods and Programs in Biomedicine,* 2010. Vol. 98 (3): pp. 261-270.

[24] Gordon, R., R. Bender, and G. T. Herman, "Algebraic Reconstruction Techniques (ART) for three-dimensional electron microscopy and X-ray photography," *Journal of Theoretical Biology,* 1970. Vol. 29 (3): pp. 471-"476,IN1-IN2,477-481".

[25] Badea, C. and R. Gordon, "Experiments with the nonlinear and chaotic behaviour of the multiplicative algebraic reconstruction technique (MART) algorithm for

computed tomography," *Physics in Medicine and Biology,* 2004. Vol. 49 (8): pp. 1455-1474.

[26] Prakash, P., et al., "Radiation dose reduction with chest computed tomography using adaptive statistical iterative reconstruction technique: Initial experience," *Journal of Computer Assisted Tomography,* 2010. Vol. 34 (1): pp. 40-45.

[27] Singh, S., et al., "Adaptive statistical iterative reconstruction technique for radiation dose reduction in chest CT: A pilot study," *Radiology,* 2011. Vol. 259 (2): pp. 565-573.

[28] Katsura, M., et al., "Model-based iterative reconstruction technique for radiation dose reduction in chest CT: Comparison with the adaptive statistical iterative reconstruction technique," *European Radiology,* 2012. Vol. 22 (8): pp. 1613-1623.

[29] Burger, M. and S. Osher, *A guide to the TV zoo*, in *Lecture Notes in Mathematics*. 2013. p. 1-70.

[30] Lange, K. and R. Carson, "EM reconstruction algorithms for emission and transmission tomography," *Journal of Computer Assisted Tomography,* 1984. Vol. 8 (2): pp. 306-316.

[31] Lange, K. and J. A. Fessler, "Globally convergent algorithms for maximum a posteriori transmission tomography," *IEEE Transactions on Image Processing,* 1995. Vol. 4 (10): pp. 1430-1438.

[32] Ma, J., "Algorithms for non-negatively constrained maximum penalized likelihood reconstruction in tomographic imaging," *Algorithms,* 2013. Vol. 6 (1): pp. 136-160.

[33] Fessler, J. A. and A. O. Hero Iii, "Penalized maximum-likelihood image reconstruction using space-alternating generalized EM algorithms," *IEEE Transactions on Image Processing,* 1995. Vol. 4 (10): pp. 1417-1429.

[34] Green, P. J., "Bayesian reconstructions from emission tomography data using a modified EM algorithm," *IEEE Transactions on Medical Imaging,* 1990. Vol. 9 (1): pp. 84-93.

[35] Candès, E. J., J. Romberg, and T. Tao, "Robust uncertainty principles: Exact signal reconstruction from highly incomplete frequency information," *IEEE Transactions on Information Theory,* 2006. Vol. 52 (2): pp. 489-509.

[36] Donoho, D. L., "Compressed sensing," *IEEE Transactions on Information Theory* 2006. Vol. 52 (4): pp. 1289-1306.

[37]   Pan, X., E. Y. Sidky, and M. Vannier, "Why do commercial CT scanners still employ traditional, filtered back-projection for image reconstruction?," *Inverse Problems,* 2009. Vol. 25 (12).

[38]   Muthukrishnan, S., "*Data Streams: Algorithmds and Applications*. 2005, Hanover, MA: Now Publishers.

[39]   Rish, I. and G. Grabarnik. "Sparse signal recovery with exponential-family noise," in *2009 47th Annual Allerton Conference on Communication, Control, and Computing*. 2009.

[40]   Tropp, J. A. and A. C. Gilbert, "Signal recovery from random measurements via orthogonal matching pursuit," *IEEE Transactions on Information Theory,* 2007. Vol. 53 (12): pp. 4655-4666.

[41]   Blumensath, T. and M. E. Davies, "Iterative hard thresholding for compressed sensing," *Applied and Computational Harmonic Analysis,* 2009. Vol. 27 (3): pp. 265-274.

[42]   Kunis, S. and H. Rauhut, "Random sampling of sparse trigonometric polynomials, II. Orthogonal matching pursuit versus basis pursuit," *Foundations of Computational Mathematics,* 2008. Vol. 8 (6): pp. 737-763.

[43]   Needell, D. and R. Vershynin, "Uniform uncertainty principle and signal recovery via regularized orthogonal matching pursuit," *Foundations of Computational Mathematics,* 2009. Vol. 9 (3): pp. 317-334.

[44]   Needell, D. and J. A. Tropp, "CoSaMP: Iterative signal recovery from incomplete and inaccurate samples," *Applied and Computational Harmonic Analysis,* 2009. Vol. 26 (3): pp. 301-321.

[45]   Gardũo, E., G. T. Herman, and R. Davidi, "Reconstruction from a few projections by ℓ1-minimization of the Haar transform," *Inverse Problems,* 2011. Vol. 27 (5).

[46]   Chen, G. H., J. Tang, and S. Leng, "Prior image constrained compressed sensing (PICCS): A method to accurately reconstruct dynamic CT images from highly undersampled projection data sets," *Medical Physics,* 2008. Vol. 35 (2): pp. 660-663.

[47]   Chen, G. H., et al., "Prior image constrained compressed sensing (PICCS) and applications in X-ray computed tomography," *Current Medical Imaging Reviews,* 2010. Vol. 6 (2): pp. 119-134.

[48]   Han, X., et al., "Optimization-based reconstruction of sparse images from few-view projections," *Physics in medicine and biology,* 2012. Vol. 57 (16): pp. 5245-5273.

[49]   Lustig, M., D. Donoho, and J. M. Pauly, "Sparse MRI: The application of compressed sensing for rapid MR imaging," *Magnetic Resonance in Medicine,* 2007. Vol. 58 (6): pp. 1182-1195.

[50]   Zhu, Z., K. A. Wahid, and P. Babyn. "CT image reconstruction from partial angular measurements via compressed sensing," in *2012 25th IEEE Canadian Conference on Electrical and Computer Engineering: Vision for a Greener Future, CCECE 2012*. 2012.

[51]   Rudin, L. I., S. Osher, and E. Fatemi, "Nonlinear total variation based noise removal algorithms," *Physica D: Nonlinear Phenomena,* 1992. Vol. 60 (1-4): pp. 259-268.

[52]   Chambolle, A., "An Algorithm for Total Variation Minimization and Applications," *Journal of Mathematical Imaging and Vision,* 2004. Vol. 20 (1-2): pp. 89-97.

[53]   Le, T., R. Chartrand, and T. J. Asaki, "A variational approach to reconstructing images corrupted by poisson noise," *Journal of Mathematical Imaging and Vision,* 2007. Vol. 27 (3): pp. 257-263.

[54]   Aujol, J. F., "Some first-order algorithms for total variation based image restoration," *Journal of Mathematical Imaging and Vision,* 2009. Vol. 34 (3): pp. 307-327.

[55]   Debatin, M., et al. "CT reconstruction from few-views by anisotropic total variation minimization," in *IEEE Nuclear Science Symposium Conference Record*. 2012.

[56]   Li, H., et al., "Sparse CT reconstruction based on multi-direction anisotropic total variation (MDATV)," *BioMedical Engineering Online,* 2014. Vol. 13 (1).

[57]   Niu, S., et al., "Sparse-view x-ray CT reconstruction via total generalized variation regularization," *Physics in Medicine and Biology,* 2014. Vol. 59 (12): pp. 2997-3017.

[58]   Liu, Y., et al., "Total variation-stokes strategy for sparse-view x-ray ct image reconstruction," *IEEE Transactions on Medical Imaging,* 2014. Vol. 33 (3): pp. 749-763.

[59]   Duan, X., et al., "Few-view projection reconstruction with an iterative reconstruction- reprojection algorithm and TV constraint," *IEEE Transactions on Nuclear Science,* 2009. Vol. 56 (3): pp. 1377-1382.

[60]   Liu, Y., et al., "Adaptive-weighted total variation minimization for sparse data

toward low-dose x-ray computed tomography image reconstruction," *Physics in Medicine and Biology,* 2012. Vol. 57 (23): pp. 7923-7956.

[61] Chartrand, R., E. Y. Sidky, and X. Pan. "Nonconvex compressive sensing for X-ray CT: An algorithm comparison," in *Conference Record - Asilomar Conference on Signals, Systems and Computers*. 2013.

[62] Bardsley, J. M. and J. Goldes, "Regularization parameter selection methods for ill-posed Poisson maximum likelihood estimation," *Inverse Problems,* 2009. Vol. 25 (9).

[63] Figueiredo, M. A. T., R. D. Nowak, and S. J. Wright, "Gradient projection for sparse reconstruction: Application to compressed sensing and other inverse problems," *IEEE Journal on Selected Topics in Signal Processing,* 2007. Vol. 1 (4): pp. 586-597.

[64] Becker, S., J. Bobin, and E. J. Candès, "NESTA: A fast and accurate first-order method for sparse recovery," *SIAM Journal on Imaging Sciences,* 2011. Vol. 4 (1): pp. 1-39.

[65] Bonettini, S. and V. Ruggiero, "On the convergence of primal-dual hybrid gradient algorithms for total variation image restoration," *Journal of Mathematical Imaging and Vision,* 2012. Vol. 44 (3): pp. 236-253.

[66] Chambolle, A. and T. Pock, "A first-order primal-dual algorithm for convex problems with applications to imaging," *Journal of Mathematical Imaging and Vision,* 2011. Vol. 40 (1): pp. 120-145.

[67] Hastie, T., et al., "The Entire Regularization Path for the Support Vector Machine," *J. Mach. Learn. Res.,* 2004. Vol. 5: pp. 1391-1415.

[68] Goldfarb, D. and W. Yin, "Second-order cone programming methods for total variation-based image restoration," *SIAM Journal on Scientific Computing,* 2006. Vol. 27 (2): pp. 622-645.

[69] Ramani, S. and J. A. Fessler, "A splitting-based iterative algorithm for accelerated statistical X-ray CT reconstruction," *IEEE Transactions on Medical Imaging,* 2012. Vol. 31 (3): pp. 677-688.

[70] Darbon, J. and M. Sigelle, "Image restoration with discrete constrained total variation part I: Fast and exact optimization," *Journal of Mathematical Imaging and Vision,* 2006. Vol. 26 (3): pp. 261-276.

[71] Se Young, C., Y. K. Dewaraja, and J. A. Fessler, "Alternating Direction Method of Multiplier for Tomography With Nonlocal Regularizers," *Medical Imaging, IEEE Transactions on,* 2014. Vol. 33 (10): pp. 1960-1968.

[72]   Leng, S., et al., "High temporal resolution and streak-free four-dimensional cone-beam computed tomography," *Physics in Medicine and Biology,* 2008. Vol. 53 (20): pp. 5653-5673.

[73]   Rouse, D. M. and S. S. Hemami. "Understanding and simplifying the structural similarity metric," in *Proceedings - International Conference on Image Processing, ICIP*. 2008.

[74]   Samei, E., M. J. Flynn, and D. A. Reimann, "A method for measuring the presampled MTF of digital radiographic systems using an edge test device," *Medical Physics,* 1998. Vol. 25 (1): pp. 102-113.

[75]   Sidky, E. Y., C. M. Kao, and X. Pan, "Accurate image reconstruction from few-views and limited-angle data in divergent-beam CT," *Journal of X-Ray Science and Technology,* 2006. Vol. 14 (2): pp. 119-139.

[76]   Wang, J., et al., "Penalized weighted least-squares approach to sinogram noise reduction and image reconstruction for low-dose X-ray computed tomography," *IEEE Transactions on Medical Imaging,* 2006. Vol. 25 (10): pp. 1272-1283.

[77]   Bouman, C. and K. Sauer, "Generalized Gaussian image model for edge-preserving MAP estimation," *IEEE Transactions on Image Processing,* 1993. Vol. 2 (3): pp. 296-310.

[78]   Kisner, S. J., et al. "Limited view angle iterative CT reconstruction," 2012.

[79]   Thibault, J. B., et al., "A three-dimensional statistical approach to improved image quality for multislice helical CT," *Medical Physics,* 2007. Vol. 34 (11): pp. 4526-4544.

[80]   Tang, J., B. E. Nett, and G. H. Chen, "Performance comparison between total variation (TV)-based compressed sensing and statistical iterative reconstruction algorithms," *Physics in Medicine and Biology,* 2009. Vol. 54 (19): pp. 5781-5804.

[81]   Egiazarian, K., A. Foi, and V. Katkovnik. "Compressed sensing image reconstruction via recursive spatially adaptive filtering," in *Proceedings - International Conference on Image Processing, ICIP*. 2006.

[82]   Huang Jing, J., et al., "Sparse angular CT reconstruction using non-local means based iterative-correction POCS," *Computers in Biology and Medicine,* 2011. Vol. 41 (4): pp. 195-205.

[83]   Tian, Z., et al., "Low-dose CT reconstruction via edge-preserving total variation regularization," *Physics in Medicine and Biology,* 2011. Vol. 56 (18): pp. 5949-5967.

[84] Herman, G. T. and R. Davidi, "Image reconstruction from a small number of projections," *Inverse Problems,* 2008. Vol. 24 (4).

[85] Sidky, E. Y., J. H. Jorgensen, and X. Pan, "Convex optimization problem prototyping for image reconstruction in computed tomography with the ChambollePock algorithm," *Physics in Medicine and Biology,* 2012. Vol. 57 (10): pp. 3065-3091.

[86] Sidky, E. Y. and X. Pan, "Image reconstruction in circular cone-beam computed tomography by constrained, total-variation minimization," *Physics in Medicine and Biology,* 2008. Vol. 53 (17): pp. 4777-4807.

[87] Chen, Z., et al., "A limited-angle CT reconstruction method based on anisotropic TV minimization," *Physics in Medicine and Biology,* 2013. Vol. 58 (7): pp. 2119-2141.

[88] Jin, X., et al. "Anisotropic total variation minimization method for limited-angle CT reconstruction," in *Proceedings of SPIE - The International Society for Optical Engineering*. 2012.

[89] Qi, H., Z. Chen, and L. Zhou, "CT Image Reconstruction from Sparse Projections Using Adaptive TpV Regularization," *Computational and Mathematical Methods in Medicine*.

[90] Ramirez-Giraldo, J. C., et al., "Nonconvex prior image constrained compressed sensing (NCPICCS): Theory and simulations on perfusion CT," *Medical Physics,* 2011. Vol. 38 (4): pp. 2157-2167.

[91] Qi, Z. and G. H. Chen, "Extraction of tumor motion trajectories using PICCS-4DCBCT: A validation study," *Medical Physics,* 2011. Vol. 38 (10): pp. 5530-5538.

[92] Craft, A. E., et al., *AFIP-7 Tomography – 2013 Status Report*. 2013. p. INL/EXT-13-30741 United States, doi: 10.2172/1124666.

[93] Sawatzky, A., et al., *Total variation processing of images with poisson statistics*, in *Lecture Notes in Computer Science (including subseries Lecture Notes in Artificial Intelligence and Lecture Notes in Bioinformatics)*. 2009. p. 533-540.

[94] Brune, C., A. Sawatzky, and M. Burger, "Primal and dual Bregman methods with application to optical nanoscopy," *International Journal of Computer Vision,* 2011. Vol. 92 (2): pp. 211-229.

[95] Zanella, R., et al., "Efficient gradient projection methods for edge-preserving removal of Poisson noise," *Inverse Problems,* 2009. Vol. 25 (4).

[96]   Je, U., et al., "Dental cone-beam CT reconstruction from limited-angle view data based on compressed-sensing (CS) theory for fast, low-dose X-ray imaging," *Journal of the Korean Physical Society,* 2014. Vol. 64 (12): pp. 1907-1911.

[97]   Zhang, Y., et al., "A comparative study of limited-angle cone-beam reconstruction methods for breast tomosynthesis," *Medical Physics,* 2006. Vol. 33 (10): pp. 3781-3795.

[98]   Gao, H., et al., "Volumetric imaging from a multisegment straight-line trajectory and a practical reconstruction algorithm," *Optical Engineering,* 2007. Vol. 46 (7): pp. 077004-077004-10.

[99]   Ren, B., et al. "Design and performance of the prototype full field breast tomosynthesis system with selenium based flat panel detector," 2005.

[100] Kolitsi, Z., G. Panayiotakis, and N. Pallikarakis, "A method for selective removal of out-of-plane structures in digital tomosynthesis," *Medical Physics,* 1993. Vol. 20 (1): pp. 47-50.

[101] Wu, T., R. H. Moore, and D. B. Kopans, "Voting strategy for artifact reduction in digital breast tomosynthesis," *Medical Physics,* 2006. Vol. 33 (7): pp. 2461-2471.

[102] Ghosh Roy, D. N., et al., "Selective plane removal in limited angle tomographic imaging," *Medical Physics,* 1985. Vol. 12 (1): pp. 65-70.

[103] Nett, B., et al. "Tomosynthesis via total variation minimization reconstruction and Prior Image Constrained Compressed Sensing (PICCS) on a C-arm system," in *Progress in Biomedical Optics and Imaging - Proceedings of SPIE*. 2008.

[104] Chan, T., et al., "*Total variation image restoration: Overview and recent developments*," in *Handbook of Mathematical Models in Computer Vision*. 2006. p. 17-31.

[105] Deng, G., "A generalized unsharp masking algorithm," *IEEE Transactions on Image Processing,* 2011. Vol. 20 (5): pp. 1249-1261.

[106] Abir, M., et al. "Multiscale based adaptive contrast enhancement," in *Proceedings of SPIE - The International Society for Optical Engineering*. 2013.

VITA

Muhammad Imran Khan Abir was born on October, 1987, in Tangail, Bangladesh. He received his Bachelor of Science in Mechanical Engineering from Bangladesh University of Engineering and Technology, Dhaka, Bangladesh in October 2009. He gained industry experience as a probationary engineer in an oil refining company, Eastern Refinery Ltd., at Chittagong, Bangladesh. Being a part of researcher, he joined at Missouri University of Science and Technology for pursuing his M.S. in Nuclear Engineering in 2010 and awarded his Master of Science degree in December 2011. He gained extensive experience in radiation imaging and digital image processing research during his Ph.D. study. His dissertation establishes the need for PIE of reactor components using computed tomography with few projections. He has 1 year of hands-on experience to work at the Idaho National Laboratory. He has also contributed to different technical proposal writing during his graduate studies. He also awarded fellowship from Idaho National Laboratory to pursue his Ph.D. research. He published several technical publications, including peer reviewed conference proceedings and technical reports. His research is submitted to peer-reviewed journals for publication. He received his Ph.D. degree in Nuclear Engineering from Missouri University of Science and Technology in August 2015.